MAGNETIC PROPERTIES OF $Mg_{1-x}Zn_xFe_2O_4$ NANOFERRITES AND TETRACYCLINE-FERRITE NANOCOMPOSITES

by

Patrick Petrus Masina

BSc (UniZul), BSc (Hons) (UWC)

This dissertation is submitted in fulfilment of the academic requirements for the degree of Master of Science in the School of Chemistry and Physics, University of KwaZulu-Natal

January 2013

Abstract

We present a systematic study of the synthesis, structural and magnetic properties of $Mg_{1-x}Zn_xFe_2O_4$ nanoferrites and that of tetracycline-$Mg_{0.5}Zn_{0.5}Fe_2O_4$ nanocomposites. The nanoferrites were synthesized by the low temperature glycol-thermal technique at 200 °C. Single phase formation and the structural properties were determined by X-ray diffraction (XRD). The Scherrer formula was used to estimate crystallite sizes which ranged from 10.60 to 22.24 nm. The method of washing the precipitates by sedimentation using a centrifuge appears to be critical on the crystallite sizes. The lattice parameters increased with increased zinc ion concentration as expected because of the larger radii of Zn^{2+} ions. A strong correlation was found between the XRD density ρ_{XRD} and x. The magnetic properties as a function of x were investigated by ^{57}Fe Mössbauer spectroscopy and by magnetization measurements using a vibrating sample magnetometer (VSM). The Mössbauer spectra show ferrimagnetism for $x \leq 0.7$ and paramagnetism for $x > 0.7$ at room temperature. A peak in the saturation magnetization was observed at $x = 0.5$. The magnetic properties of the mixed Mg-Zn nanoferrites were more enhanced compared to the parent compounds of $MgFe_2O_4$ and $ZnFe_2O_4$ nanoferrites.

Nanocomposites of tetracycline-$Mg_{0.5}Zn_{0.5}Fe_2O_4$ were also synthesized by high-energy ball milling. The pre-mixed starting materials (tetracycline hydrochloride and $Mg_{0.5}Zn_{0.5}Fe_2O_4$) were milled for 1, 3, 5, 15 and 30 h under air and argon atmospheres. The resulting nanocomposites had well defined cubic spinel for both atmospheres. The crystallite sizes increased with milling time, a trend that is not so familiar with milling. A larger average crystallite size of about 39 nm was obtained after 30 h of milling of the nanocomposite in the air. Less variation and more stability was observed for samples milled in argon. The magnetic properties were enhanced by milling as confirmed by the decreased doublet areas by further milling. Hyperfine fields at tetrahedral (A) sites appear to be more responsive to further milling and hence we suspect that the tetracycline to be complexing more with ions at A sites. These results appear to have an important effect in the enhancement of the bioactivity of tetracycline.

Declaration

Plagiarism

I, PATRICK PETRUS MASINA declare that

1. The research reported in this dissertation, except where otherwise indicated, is my original research.

2. This dissertation has not been submitted for any degree or examination at any university.

3. This dissertation does not contain other person's data, pictures, graphs or other information, unless specifically acknowledged as being sourced from other persons.

4. This dissertation does not contain other persons writings, unless specifically acknowledged as being sourced from other researchers. When other written sources have been quoted, then:

   (a) Their words have been re-written but general information attributed to them has been referenced.

   (b) Where their exact words have been used, their writing has been placed in italics and inside quotation, and referenced.

5. This dissertation does not contain text, graphics or tables copied and pasted from internet, unless specifically acknowledged, and the source being detailed in the dissertation and in the reference sections.

Signed: ....

Publications based on current work

1. Tetracycline-ferrite nanocomposites formed via high-energy milling and the influence of milling conditions, M. L. Branham, T. Moyo, H. M. I. Abdallah and **P. Masina**, European Journal of Pharmaceutics and Biopharmaceutics, DOI: 10.1016/j.ejpb.2012.09.017.

2. Synthesis, characterization and magnetic properties of $Mg_{1-x}Zn_xFe_2O_4$ nano-ferrites, **P. Masina**, T. Moyo and H. M. I. Abdallah (In preparation 2013).

Dedication

I dedicate this thesis to my supportive wife Zandile and my children Sakhile, Prince and Simphiwe.

Acknowledgements

I would like to express my gratitude to my supervisor Dr. Thomas Moyo for giving me a chance to do this project. His continuous support, guidance and words of encouragement gave me strength to complete this project. My special thanks go to Dr. Hafiz Abdallah for his unlimited help from day one. I would also like to thank Dr. Michael Branham for his collaboration which made this study to be a success. He introduced me to interesting applications of nanoferrites. My sincere thanks also go to Dr. Justice Msomi for his encouraging words of support. Finally I would like to thank my colleagues Dr. Nkanyiso Mbatha, Prince Mkwae, Bheki Zulu, Thabo Mweli, Aphelele Mgabisa, Simphiwe Mathenjwa and Tondani Mboneni for all their usual friendship and encouragement.

Contents

List of Figures

List of Tables

Chapter 1

Introduction

1.1 A brief overview on ferrites

Ferrites are a group of oxides with their metal cations forming two sublattices, namely the tetrahedral (A) and the octahedral (B) crystallographic sites [1]. The oxides have a spinel crystal structure with chemical composition of the form AB_2O_4 where A and B are a single or a combination of divalent or trivalent metal ions which occupy A and B sites [2]. $M\text{Fe}_2\text{O}_4$ where M = Mg, Cd, Zn and Ni are examples of simple ferrites [3] and $\text{Mg}_{0.5}\text{Zn}_{0.5}\text{Fe}_2\text{O}_4$ is an example of a mixed ferrite. In the present study we have investigated the structural and magnetic properties which result from the addition of non-magnetic ions like Zn^{2+} to the MgFe_2O_4 spinel oxide. Ferrites can be produced in bulk or nanoparticle form with a variety of magnetic and electrical properties which render them useful or attractive for many practical applications. Ferrites possess the combined properties of magnetic materials and insulators. The variation in properties is influenced by several factors such as the cations involved, their distribution amongst the crystallographic sites, synthesis method and sintering time. In this chapter we present a brief discussion of the structure, synthesis, magnetic properties and interesting applications of these novel materials. The main aims and objectives of the study and a brief outline of the dissertation are also given.

1.2 Crystal structure

Ferrites have the crystal structure of the mineral spinel ($MgAl_2O_4$) and have the general chemical formula MFe2O4 where Fe ions replace the Al ions and M is a divalent metal ion [4]. All ferrites are man-made except for the only naturally occurring magnetite ($Fe^{2+}Fe_2^{3+}O_4$) which is also referred to as ferrous ferrite. In the spinel structure, the larger oxygen ions are packed close together in a face-centered cubic arrangement forming smaller spaces between them which can be occupied by the smaller metal ions [5]. In Figure 1.1 we show a unit cell of a spinel structure. Two types of spaces with different environments are formed between the oxygen ions. One is the center of a tetrahedron whose corners are occupied by oxygen ions. The other center is an octahedron.

Depending on the cations distribution amongst the interstitials sites the structure is referred to as 'normal' or 'inverse' spinel. In a normal spinel, all the divalent ions (A^{2+}) occupy the tetrahedral sites and the octahedral sites are occupied by the trivalent ions (Fe^{3+}). $ZnFe_2O_4$ and $CdFe_2O_4$ are perfect examples of normal spinels [5]. In an inverse spinel ferrite, all the divalent ions occupy the octahedral sites and the trivalent ions are equally distributed at both the tetrahedral and octahedral sites. Some popular examples of inverse spinel ferrites are $NiFe_2O_4$ and $CuFe_2O_4$ [6]. However, it is not always the case that a perfectly normal or inverse spinel structure is obtained. Most ferrites are either partially normal or partially inverse. These intermediate structures between the normal and inverse spinel structures can be characterized by a degree of inversion λ. In such cases the cations distributions amongst the tetrahedral and octahedral sites can be expressed by $(M_{1-2\lambda}Fe_{2\lambda})[M_{2\lambda}Fe_{2(1-\lambda)}]O_4$ where the normal brackets represent the A site and the square brackets represent the B site. The value of λ tends to be temperature-dependent ranging from 0 to 0.5 with $\lambda = 0$ assigned to a normal spinel and $\lambda = 0.5$ assigned to inverse spinel [7]. Examples of partially inverse ferrites are $MgFe_2O_4$ and $MnFe_2O_4$. Mixed ferrites can also be produced where M in the structure is a combination of two or more divalent ions. Some common examples of mixed ferrites are Mg-Zn, Ni-Zn and Co-Ni ferrites. Most commercially used ferrites are mixed.

(a) Tetrahedral A site   (b) Octahedral B site

- Metal ion in tetrahedral site
- Metal ion in octahedral site
- Oxygen ion

(c)

(d)
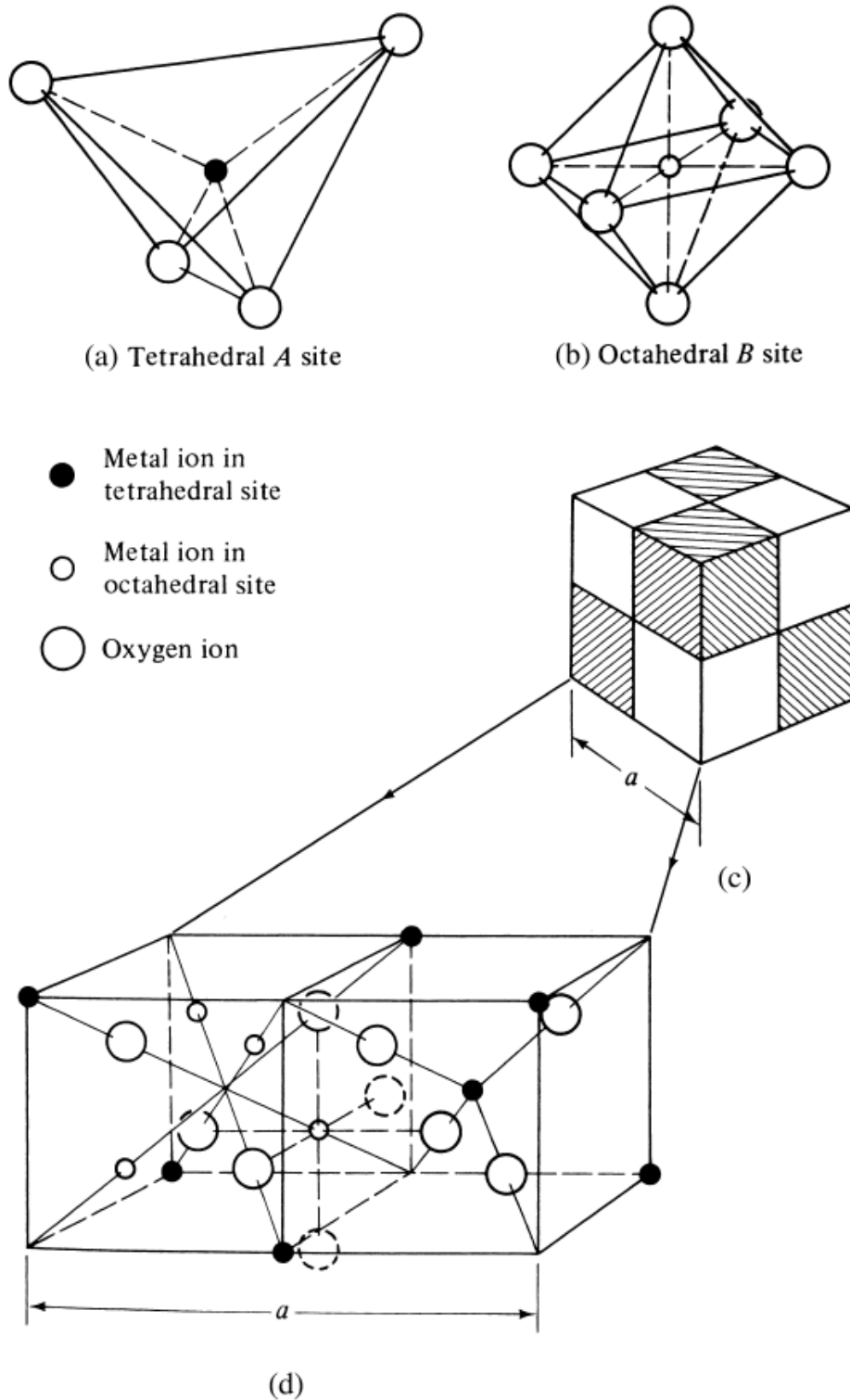
Figure 1.1: Crystal structure and metal ion occupations of the tetrahedral (A) and octahedral (B) sites of a cubic spinel ferrite [5].

3

Hence the properties of the spinel material will be dependent on the cation distribution at the interstitial sites. This is found to be influenced by the synthesis methods.

1.3   Synthesis

Ferrites exhibit different properties because of different factors such as constituent ions and synthesis methods. The key factor in obtaining good quality samples is by selecting an appropriate synthesis technique. High purity starting oxides can be used to prepare ferrites in the bulk form by the solid state reaction (ceramic method). The main disadvantage of this method is the prolonged heat treatments at high temperature [6]. The elevated temperatures more likely cause some of the constituent materials to evaporate and thus cause the unbalancing of the stochiometry [8]. During the grinding process in the conventional ceramic method, some sample is lost by sticking to the grinding surfaces resulting in a non-stochiometric composition. The grinding or milling process may also introduce impurities from the grinding material into the final product. A wide range of particle sizes are also obtained by mechanical milling which may produce samples with irreproducible characteristics.

The wet chemical techniques serve as a better alternative to the solid state reaction because samples with a high level of homogeneity can be produced at a low sintering temperature [9, 10]. A variety of these wet chemical methods are available such as hydrothermal, glycol-thermal, sol-gel, combustion and co-precipitation [11, 12, 13, 14]. Here, metal chloride or nitrate salt solutions for a desired composition are mixed by continuous stirring to allow mixing at atomic level to take place. A base such as ammonium hydroxide (NH_4OH) for chlorides or potassium hydroxide (KOH) for nitrates is added to the mixture to form a precipitate. Surfactants may also be added to the mixture in order to limit crystal growth [15]. The precipitate is then dispersed in deionised water or ethylene glycol and heated to allow further reaction to take place. The mixture is then filtered and dried. Further sintering may be performed at much lower temperature compared to the solid state reaction technique to ensure the formation of single phase material. The ferrites produced

by the wet chemistry techniques are of high purity as the incorporation of unwanted impurities is significantly reduced.

1.4   Magnetic properties

In this section we briefly discuss the magnetic order in ferrites that make them useful in various applications. The magnetic properties are determined by the magnetic interactions between magnetic moments which are strongly dependent on the location of metal cations in the crystal structure. The interaction of the cations is mediated by the oxygen ions which also insulate them from each other and thus resulting in high resistivity as another important property of ferrites. The interaction between magnetic moments via the intermediary oxygen ions is referred to as superexchange interaction which is the source of magnetism in ferrites. Since the magnetic moments of the cations occupying the A and B sites are not equal, the strong superexchange interactions results in an anti-parallel arrangement with net non-zero magnetization [16]. This type of magnetic ordering is known as ferrimagnetism. This is similar to ferromagnetic order. Spontaneous ordering of the magnetic moments occurs below the Curie temperature T_C. However, significant positive and negative exchange interactions occur in ferrimagnets. In some ferrimagnets the net magnetization can also be zero at a temperature below T_C called the compensation temperature T_{comp} [17]. More details of the different types of magnetic order in solids are given in the next chapter.

1.5   Applications

Ferrites have been widely used in a wide range of applications due to their favourable magnetic, electrical and mechanical properties such as in high-density data storage, magnetocaloric refrigeration, magnetic resonance imaging (MRI) and drug delivery [18, 19, 20, 21]. Mn-Zn ferrites have high permeability, high saturation magnetization and low core losses. They are used in high frequency devices such as mobile phones, transformers, radios and magnetic heads [22]. The Mn-Zn ferrites are also

5

potential candidates in the asymmetric digital subscriber line application (ADSL) where fast data transfer is required [23]. Ni-Zn ferrites have high permeability and resistivity so they are useful in radio-frequency (RF) applications such as low loss inductors, transformer cores and electromagnetic interference suppression devices at high frequencies [24]. Magnesium ferrites have been used as catalysts and humidity sensors. Superparamagnetic ferrites have also have also become promising candidates for biomedical applications in magnetic carrier technology (MCT) for selective extraction of biological components and drug delivery to specific parts of the body [25]. The heating effects of magnetic nanoparticles in response to alternating magnetic field has also been used in the treatment of cancer using hyperthermia [26].

1.6   Motivation for the current work

The magnetic properties of ferrites is influenced by the cation distribution amongst the interstitial sites. The synthesis method, composition, sintering time and sintering temperature are factors which determine the cation distribution and hence the magnetic properties. Ionic sizes and cation valency also play a role in the cation distributions [27]. Ni-Zn ferrites have been widely used in industry because of their unique properties. The US environmental protection Agency for Toxic Substances and Disease Registry (ATSDR) and US Department of Health and Human Services have identified nickel and its compounds as human carcinogens [28, 29]. We were also motivated by the use of Mg-Zn ferrites as a low-toxicity alternative to the Ni-Zn ferrites [24]. It is therefore important to investigate the variation of the structural and magnetic properties of the Mg-Zn system as a function of composition. We have therefore produced and studied structural and magnetic properties of $Mg_{1-x}Zn_xFe_2O_4$ nanoferrites for $0.0 \leq x \leq 1.0$ in steps of 0.1. High saturation magnetization (M_S) have been reported for small concentration of Zn^{2+} ions [27]. Observing the trend in M_S as a function in x can also help in confirming the site preference of the Zn^{2+} ions in Mg-Zn ferrites. [57]Fe Mössbauer spectroscopy is therefore an ideal tool in the study of such a series of compounds.

One of the compositions was selected and complexed with tetracycline-HCl via high-energy ball milling with the intention of improving the bioactivity of tetracycline against a range of bacteria. In the present work we explore the structural and magnetic properties of such nanocomposites as a function of milling time and atmosphere.

1.7   Dissertation outline

The dissertation is organized into 6 chapters. In Chapter 1 we have introduced spinel ferrites and briefly discussed their crystal structure, synthesis techniques, magnetic properties and their potential applications. Chapter 2 gives the basic theory that describes the magnetic order in solids. The experimental techniques used in this study are discussed in Chapter 3. This also include some basic literature on Mössbauer spectroscopy which is the main analytic tool used in this study. The results are presented in Chapters 4 and 5. The general conclusions of the study are presented Chapter 6.

Chapter 2

Magnetism and magnetic order in Solids

This chapter gives some background information on magnetism in materials and its origin. It is important to understand the ordering of magnetic moments in materials as they are responsible for the magnetic behavior under various conditions such as temperature and applied magnetic fields. We also give a brief discussion of the different types of magnetic order in solids. This background information is helpful in understanding and analyzing the magnetic properties of the materials under investigation in Chapters 4 and 5.

2.1   Origin of magnetism

The circular motion of electrons around the nucleus and their intrinsic spin result in the existence of magnetic moments. The moments can be permanent or induced under the effect of a magnetic field. Magnetism originates from the existence of these permanent and induced magnetic moments on constituent atoms and their mutual interactions. To illustrate the existence of a magnetic moment we consider an electron of mass m_e moving in a closed orbit of radius r as shown in Figure 2.1. The current I constituted by the moving electron is associated with a magnetic moment defined as
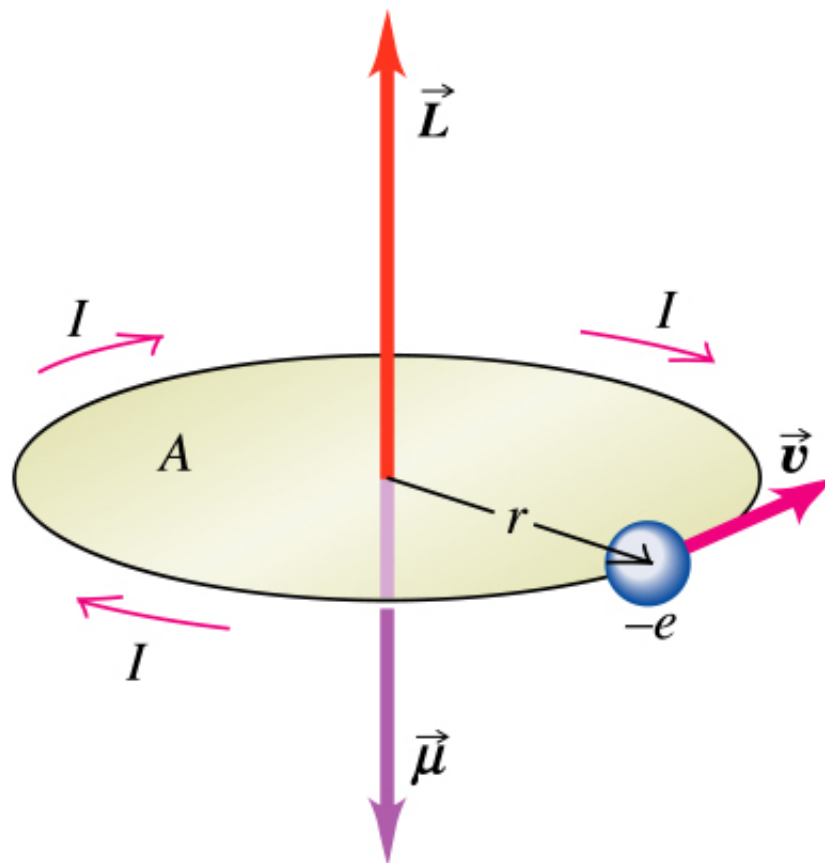
Figure 2.1: An electron moving in a close orbit [30]

$$\boldsymbol{\mu} = I\boldsymbol{A} \tag{2.1.1}$$

where $\boldsymbol{A}$ is the area of the closed loop with a magnitude of πr^2. If the electron moves with an angular speed ω then

$$I = -ef = -\frac{e\omega}{2\pi} \tag{2.1.2}$$

where f is the frequency of the rotation. The magnetic moment becomes

$$\boldsymbol{\mu} = -\frac{er^2}{2}\boldsymbol{\omega} = -\frac{em_e r^2}{2m_e}\boldsymbol{\omega} = -\frac{e}{2m_e}\boldsymbol{l} \tag{2.1.3}$$

where $\boldsymbol{l}$ is the orbital angular momentum given by $m_e r^2 \boldsymbol{\omega}$. The scalar value of the magnetic moment in the z-direction is thus given by

$$\mu_{L_z} = -\frac{e}{2m_e}l_z. \tag{2.1.4}$$

In Quantum Mechanics the angular momentum of an electron is quantized in units of $\hbar$ since $l_z = m_l \hbar$ where $m_l = 0, \pm 1, \pm 2 \dots$ Hence

$$\mu_{l_z} = -\left(\frac{e\hbar}{2m_e}\right)m_l = -\mu_B m_l. \tag{2.1.5}$$

The quantity $\mu_B = \frac{e\hbar}{2m_e} = 9.274 \times 10^{-24}$ J/T is the smallest non-zero fundamental value of μ known as the Bohr magneton. The magnetic moment due to the intrinsic spin of an electron is given by

$$\boldsymbol{\mu}_s = -\frac{e}{2m_e}g\boldsymbol{s} \tag{2.1.6}$$

where g is the Landé g factor which has an experimental value of 2.002322 for pure electron spin [31] and $\boldsymbol{s}$ is the spin angular momentum. The magnetic moment due to intrinsic spin is also quantized in units of $\hbar$, where $s_z = m_s \hbar$ and $m_s = \pm\frac{1}{2}$. Hence

$$\mu_{s_z} = -\left(\frac{e\hbar}{m_e}\right)m_s = -\mu_B g m_s. \tag{2.1.7}$$

The total magnetic moment of an electron is therefore proportional to the total angular momentum $\boldsymbol{j}$ in the form of

$$\boldsymbol{\mu} = \gamma\boldsymbol{j} = \gamma(\boldsymbol{l} + \boldsymbol{s}) \tag{2.1.8}$$

10

where γ is called the magnetomechanical ratio. For pure orbital motion ($\boldsymbol{s} = 0$), $\gamma = -\frac{e}{2m_e}$ and for pure electron spin ($\boldsymbol{l} = 0$), $\gamma = -\frac{e}{m_e}$.

The magnetic moment of an atom is determine by the collective contribution of orbital and spin angular momenta of all the individual electrons. According to the Russell-Saunders coupling, the orbital angular momenta of the electrons in an atom couple to give a resultant orbital momentum $\boldsymbol{L} = \sum\limits_{i=1}^{n} \boldsymbol{l}_i$ [32]. Similarly the resultant spin angular momentum $\boldsymbol{S} = \sum\limits_{i=1}^{n} \boldsymbol{s}_i$. The total angular momentum of an atom $\boldsymbol{J}$ is taken as the coupling of $\boldsymbol{L}$ and $\boldsymbol{S}$ through spin-orbit interaction. Using Hund's rules, the magnitude of the magnetic moment of an atom can be shown to be

$$\mu_J = \mu_B g \sqrt{J(J+1)} \tag{2.1.9}$$

where the g factor for a free atom is given by [6, 31, 33]

$$g = 1 + \frac{J(J+1) + S(S+1) - L(L+1)}{2J(J+1)}. \tag{2.1.10}$$

2.2 Magnetization and susceptibility

The total magnetic moments per unit volume of a sample is known as the magnetization $\boldsymbol{M}$ which is expressed as

$$\boldsymbol{M} = \frac{1}{V} \sum\limits_{i=1}^{n} \boldsymbol{\mu}_i. \tag{2.2.1}$$

V is the volume of a sample of mass m. The magnetization depends on temperature and the coupling between the magnetic moments. It is practically easier to measure the mass of the sample than its volume. The volume of a sample can also undergo thermal expansion and magnetostriction effects. Hence it is more convenient to measure the magnetization per unit mass which can be expressed by

$$\boldsymbol{\sigma} = \frac{1}{m} \sum\limits_{i=1}^{n} \boldsymbol{\mu}_i. \tag{2.2.2}$$

Externally applied magnetic fields can be used to stimulate the magnetic moments to align with the field. The magnetization is determined experimentally under the influence of a magnetic field H_0 which is related to the magnetic induction $B_0 = \mu_0 H_0$

where μ_0 is the permeability of free space. The degree of the magnetization of a material in response to an applied magnetic field is known as the susceptibility χ defined by

$$\chi = \frac{\mu_0 M}{B_0}. \qquad (2.2.3)$$

Materials can be classified simply according to their bulk susceptibilities. Figures 2.2 and 2.3 show the variation of the reciprocal susceptibility with temperature for different materials. Materials with induced dipole moments have negative χ and are called diamagnets [31]. There is also a variety of substances characterized by positive χ which are associated with permanent magnetic moments.

2.3 Magnetic order in solids

This section is dedicated to different types of magnetic order in solids. We explore how the magnetic moments respond to external magnetic fields and temperature change.

2.3.1 Paramagnetism

Paramagnetism occurs in atoms and molecules which have permanent magnetic moments. This occurs in materials with atoms and ions with partly filled inner d and f shells such as transition metal, rare earth and actinide elements [31]. This magnetic order is characterized by a random orientation of magnetic moments. Paramagnetism is associated with non-interacting or weakly interacting magnetic moments. The corresponding susceptibility is positive and temperature dependent. In the presence of an external magnetic field, the magnetic moments align themselves towards the direction of the field. The magnetic field intensity B_0 causes the splitting of energy levels to

$$E_J = -\boldsymbol{\mu}_J.\boldsymbol{B}_0 = -g m_J \mu_B B_0 \qquad (2.3.1)$$

where m_J is the azimuthal quantum number with values $-J, -J+1, ...J-1, J$. The average magnetic moment of an atom in the field direction is given by

$$< \mu_J > = \sum g m_J \mu_B P(E_J) \qquad (2.3.2)$$
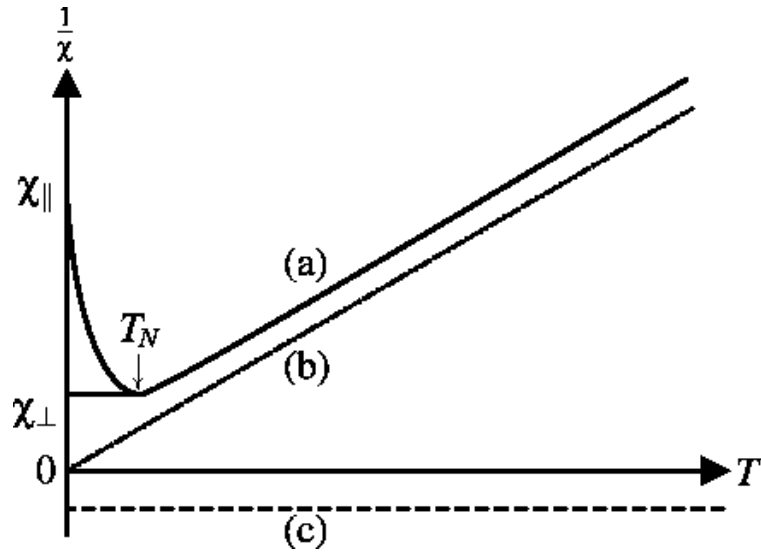
Figure 2.2: Reciprocal susceptibilities as a function of temperature for (a) antifero-magnetic, (b) paramagnetic and (c) diamagnetic materials [34].
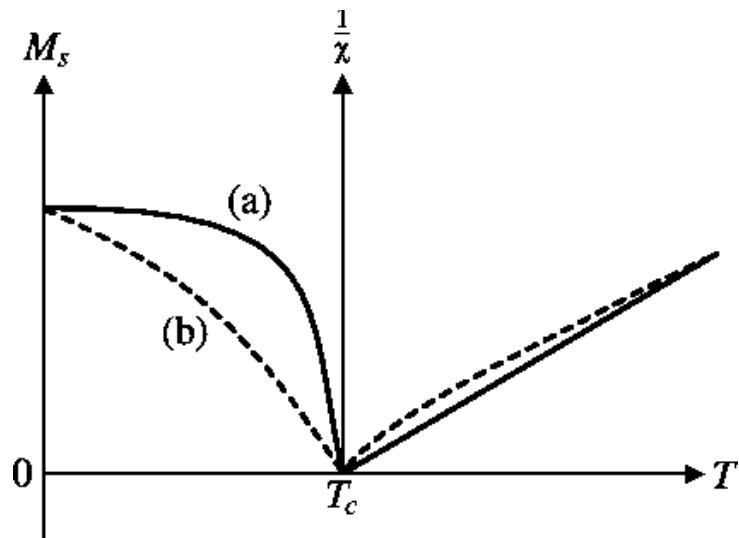
Figure 2.3: Saturation magnetization below T_C and reciprocal susceptibility above T_C for (a) ferromagnetic and (b) ferrimagnetic materials [34].

where $P(E_J)$ is the probability for the occupation of a particular energy level E_J. $P(E_J)$ is given by the Maxwell-Boltzmann distribution

$$P(E_J) = \frac{e^{-g\mu_B m_J B_0/k_B T}}{\sum e^{-g\mu_B m_J B_0/k_B T}} \tag{2.3.3}$$

where k_B is the Boltzmann constant. The average magnetic moment is thus given by

$$<\mu_B> = g\mu_B J F(J, x) \tag{2.3.4}$$

where $F(J, x)$ is the Brillouin function defined as

$$F(J, x) = \left(1 + \frac{1}{2J}\right)\coth\left[\left(1 + \frac{1}{2J}\right)x\right] - \frac{1}{2J}\coth\left(\frac{x}{2J}\right). \tag{2.3.5}$$

The parameter x is a dimensionless ratio of the Zeeman energy to the thermal energy given by

$$x = \frac{g\mu_B J B_0}{k_B T}. \tag{2.3.6}$$

For high temperature ($T \sim 300$ K) and low field ($B_0 \sim 1$ T), x becomes very small ($x << 1$) such that the Brillouin function is approximated by

$$F(J, x) \simeq \frac{x(J + 1)}{3J}. \tag{2.3.7}$$

For n non-interacting magnetic moments per unit volume, the magnetization becomes

$$M = \frac{ng_2\mu_B^2 J(J + 1)B_0}{3k_B T}. \tag{2.3.8}$$

Since the susceptibility is given by

$$\chi = \frac{\mu_0 M}{B_0} \tag{2.3.9}$$

and when substituting for M we get

$$\chi = \frac{n\mu_0 g^2 \mu_B^2 J(J + 1)}{3k_B T} = \frac{C}{T}. \tag{2.3.10}$$

This is known as the Curie law for susceptibility where

$$C = \frac{n\mu_0 g^2 \mu_B^2 J(J + 1)}{3k_B}. \tag{2.3.11}$$

C is called the Curie constant. However, in many instances interactions between magnetic moments occur which lead to the Curie-Weiss law expressed by

$$\chi = \frac{C}{T - \theta_p}. \tag{2.3.12}$$

θ_p is known as the paramagnetic Curie temperature. In presenting experimental data it is common to plot χ^{-1} against T as in Figures 2.2 and 2.3. The randomly oriented magnetic moments in a paramagnet are illustrated in Figure 2.4.

2.3.2 Ferromagnetism

Atoms of ferromagnetic materials possess magnetic moments which are spontaneously aligned below some critical temperature called the Curie temperature T_C. This occurs because of strong interaction between magnetic moments. The magnetic moments are in a parallel alignment at $T = 0$ K as shown in Figure 2.5. Examples of classical ferromagnets are Fe, Ni and Co. Even in the absence of an applied field, ferromagnets exhibit a net spontaneous magnetization. Increasing the thermal energy of the magnetic moments results in spin disorder due to thermal agitation. At the Curie temperature, the disorder of magnetic moments becomes complete. At $T > T_C$, a ferromagnet exhibits properties of a paramagnet with a susceptibility that obeys the Curie-Weiss law. However, the laws fails in the vicinity of T_C. The susceptibility near T_C is thus approximated by $\chi \sim (T - T_C)^{-\gamma}$ when approaching T_C from above and $\chi \sim (T_C - T)^{\beta}$ when approaching T_C from below. The parameters γ and β are called critical exponents and are calculated to be 1 and 0.5 respectively in the mean-field approximation [35]. The variation of the magnetization with temperature as shown in Figure 2.3 was first explained by the Wiess mean-field theory in 1907. The theory assumes the existence of an internal magnetic field B_{in} within the material which is responsible for the spontaneous alignment of magnetic moments. The spontaneous magnetization is taken to be proportional to B_{in}. Hence

$$B_{in} = \lambda M_s \tag{2.3.13}$$

where λ is referred to as the molecular field coefficient. Exchange interactions introduced in Quantum Mechanics are known to be responsible for the existence of B_{in}.
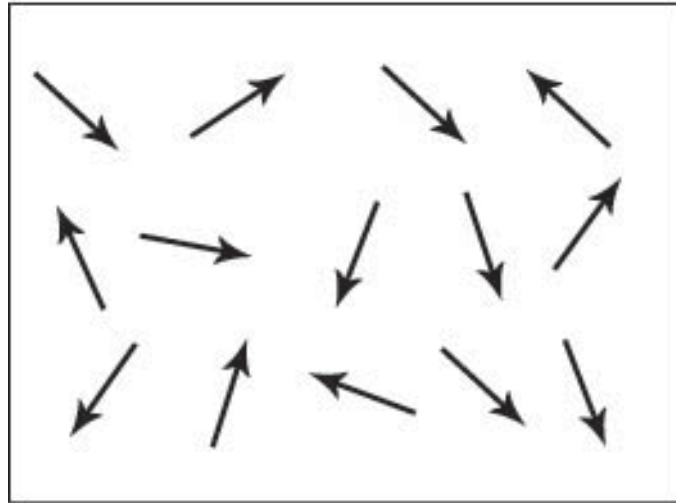
Figure 2.4: Randomly ordered magnetic moments in a paramagnetic material [36].
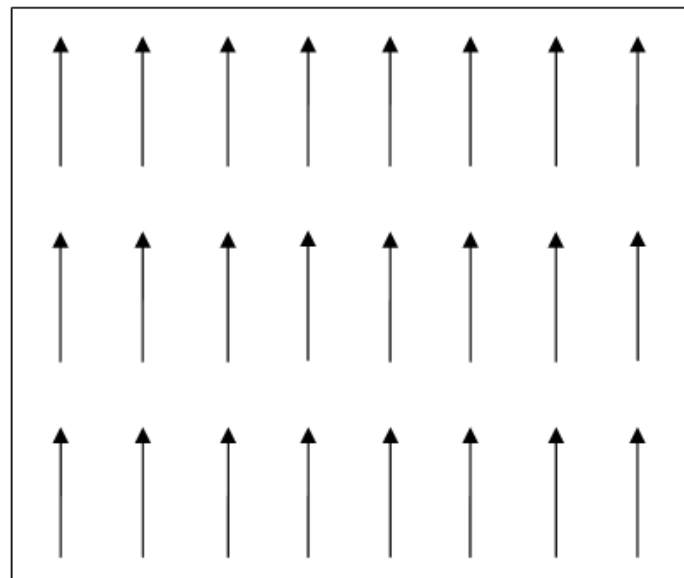
Figure 2.5: Parallel alignment of magnetic moments in a ferromagnetic material [37].

The internal field can be approximately estimated from the magnetic binding energy $\mu_B B_{in}$ and the thermal energy $k_B T_C$. The magnetic binding energy is responsible for the perfect alignment of moments at $T = 0$ K. At T_C where the magnetic order collapses, $k_B T_C \sim \mu_B B_{in}$ hence

$$B_{in} \sim \frac{k_B T_C}{\mu_B}. \tag{2.3.14}$$

B_{in} turns out to be much larger than the field that can be produced due to dipole fields of a permanent magnet ($B_{in} \sim 150$ Telsa for $T_C \sim 100$ K).

In the presence of an external applied magnetic field, the effective magnetic field in a sample is expressed by

$$B_{eff} = B_0 + B_{in} = B_0 + \lambda M_s. \tag{2.3.15}$$

Similar to a paramagnet the magnetization of a ferromagnet in an applied field can be described in terms of the Brillouin function such that

$$M_s(B_0, T) = ng\mu_B JF(J, y) \tag{2.3.16}$$

where the ratio of the Zeeman energy to thermal energy is now defined as

$$y = \frac{g\mu_B J(B_0 + \lambda M_s)}{k_B T}. \tag{2.3.17}$$

The magnetization still stays finite even for $B_0 = 0$ since $B_{in} >> B_0$. At absolute zero temperature ($T = 0$ K), the spontaneous magnetization per unit volume saturates to

$$M_s(0, 0) = ng\mu_B J. \tag{2.3.18}$$

For zero applied field ($B_0 = 0$) and $T > 0$, the spontaneous magnetization of a ferromagnet can be expressed by

$$M_s(0, T) = M_s(0, 0)F(J, y) \tag{2.3.19}$$

where in this case y is given by

$$y = \frac{g\mu_B J\lambda M_s(0, T)}{k_B T}. \tag{2.3.20}$$

17

The magnetic state of a ferromagnetic material can therefore be described by satisfying two simultaneous equations of reduced magnetizations namely

$$\frac{M_s(0,T)}{M_s(0,0)} = F(J,y) \qquad (2.3.21)$$

and

$$\frac{M_s(0,T)}{M_s(0,0)} = \left(\frac{k_B T}{n g^2 \mu_B^2 \lambda J^2}\right) y. \qquad (2.3.22)$$

Figure 2.6 shows the variation of the reduced magnetizations as a function of y. Equation (2.3.22) is represented by curve C1. The point of intersect (P) between C1 and the Brillouin function defines the magnetic state of the material. At temperatures above T_C, the assumption that $B_{in} >> B_0$ is no longer valid. The magnetic moments are now randomly oriented. This means that the sample behaves like a paramagnet above T_C. The susceptibility of a paramagnetic material above T_C is given by the Curie-Weiss law

$$\frac{C}{T - \theta_p} \qquad (2.3.23)$$

because significant interactions between the magnetic moments still exist. For many materials, experiments show that $\theta_p \geq T_C$.

The variation of the magnetization at temperatures lower than the Curie point ($T < T_C$) can also been studied. Just below T_C the reduced magnetization can be approximated by

$$\frac{M_s(T)}{M_s(0)} = \left(1 - \frac{T}{T_C}\right)^{\frac{1}{2}}. \qquad (2.3.24)$$

The Weiss theory successfully predicts the collapse of the magnetization at T_C, unfortunately the theory cannot account for the origin of the internal field and the reduction in magnetization with increasing temperature for $T << T_C$. Experimentally we find that the reduced magnetization follows the Bloch $T^{3/2}$ power law due to excitation of spin waves. The origin of internal field is now known to be due to exchange interactions [17].
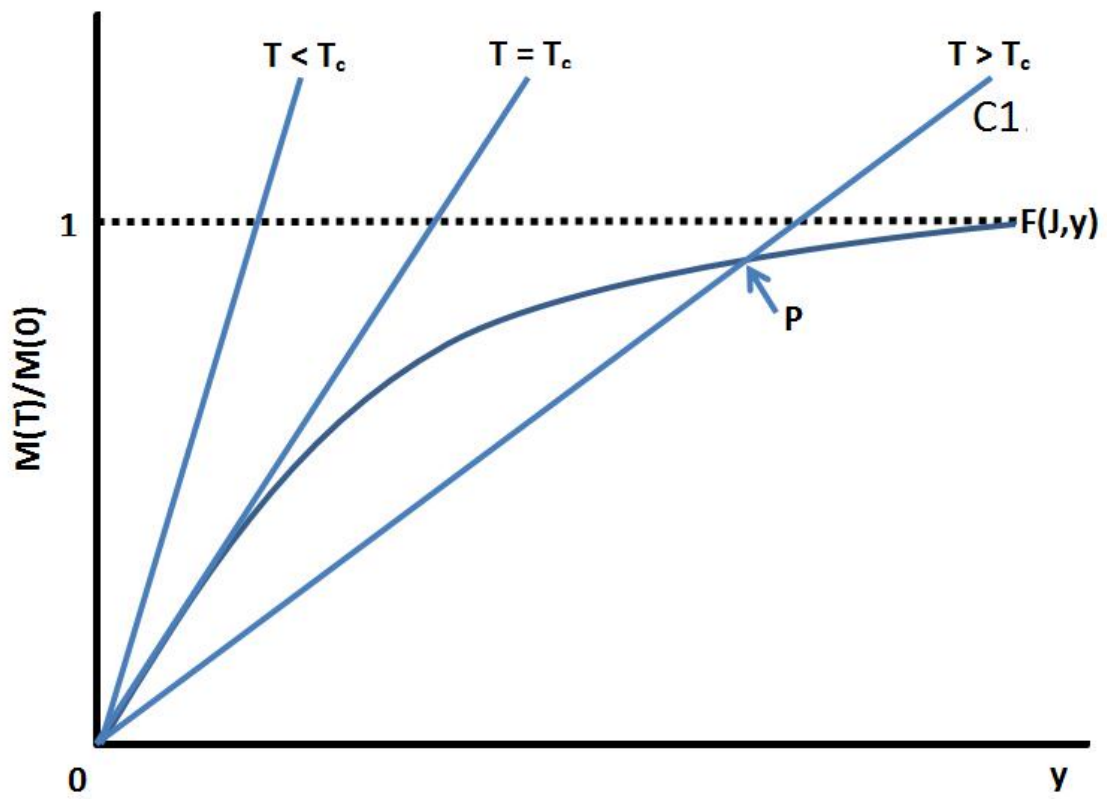
Figure 2.6: Graphical presentation of equations (2.3.21) and (2.3.22) [38].

2.3.3 Antiferromagnetism

In antiferromagnetic materials, the magnetic moments are spontaneously aligned in antiparallel orientation with zero net magnetization [31]. Figure 2.7 shows the arrangement of magnetic moments in an antiferromagnet. The antiparallel alignment of moments is observed only below the ordering temperature known as the Néel temperature T_N. The magnetic structure in an antiferromagnet is subdivided into two atomic sublattices A and B with saturation magnetization M_A and M_B respectively. The arrangement of the moments is in such a way that A atoms have only B atoms as their nearest-neighbors. Antiferromagnetism is due to negative exchange interactions [17]. For $T < T_N$, the net saturation magnetization of an antiferromagnet is zero due to the direct cancellation of $\boldsymbol{M}_A$ and $\boldsymbol{M}_B$ since $\boldsymbol{M}_A = -\boldsymbol{M}_B$. At absolute zero temperature ($T = 0$ K), each sublattice has maximum saturation magnetization which decreases with increase in temperature as in a ferromagnet. A small cusp is observed in the susceptibility of an antiferromagnet [31]. Above T_N, the magnetic moments at both sublattices are randomly orientated. This means that an antiferromagnet behaves like a paramagnet at temperatures above T_N.

The magnetization at each sublattice can be deduced using the mean-field theory and the assumption of the existence of an internal magnetic field B_{in} as in a ferromagnet. The internal field mediating the magnetic order is assumed to be due to the interaction of magnetic moments with its first and second nearest neighbors. The internal magnetic field at the respective sublattices is given by

$$\boldsymbol{B}_{in}^A = \lambda_{AA}\boldsymbol{M}_A + \lambda_{AB}\boldsymbol{M}_B \qquad (2.3.25)$$

and

$$\boldsymbol{B}_{in}^B = \lambda_{BA}\boldsymbol{M}_A + \lambda_{BB}\boldsymbol{M}_B. \qquad (2.3.26)$$

The molecular field coefficients λ_{AB} and λ_{BA} correspond to the first nearest neighbors. The second nearest neighbor molecular field coefficients are given by λ_{AA} and λ_{BB} respectively. As a matter of fact we expect

$$\lambda_{AB} = \lambda_{BA} = -\lambda_1 \qquad (2.3.27)$$

20
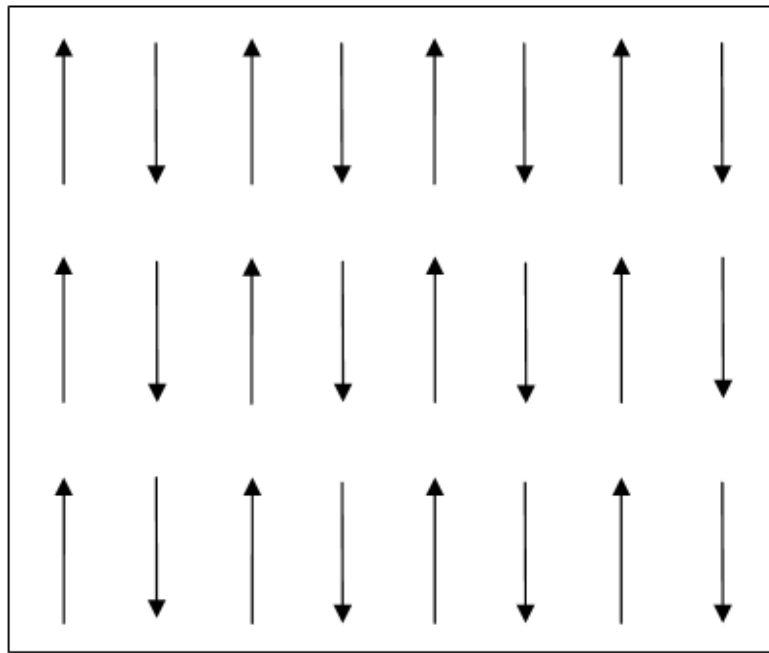
Figure 2.7: Antiparallel alignment of magnetic moments in an antiferromagnetic material.

and

$$\lambda_{AA} = \lambda_{BB} = \lambda_2 \tag{2.3.28}$$

where λ_1 and λ_2 are both positive constants. Therefore, equations (2.3.25) and (2.3.26) can be rewritten in the form of

$$\boldsymbol{B}_{in}^{A} = \boldsymbol{M}_A(\lambda_1 - \lambda_2) \tag{2.3.29}$$

and

$$\boldsymbol{B}_{in}^{B} = \boldsymbol{M}_B(\lambda_1 - \lambda_2) \tag{2.3.30}$$

respectively. The magnetization at each sublattice is now given by

$$M_i(T) = \frac{n}{2}g\mu_B J F(J, y_i) \tag{2.3.31}$$

where i is the identity of the sublattice (A or B) and

$$y_i = \frac{g\mu_B J B_{in}^i}{k_B T}. \tag{2.3.32}$$

If we let $\lambda = \lambda_1 - \lambda_2$, we can shown that the magnetization at each sublattice is given by

$$M_i(T) = \frac{n}{2}g\mu_B J F(J, y) \tag{2.3.33}$$

where y is now defined by

$$y = \frac{g\mu_B J \lambda M}{k_B T}. \tag{2.3.34}$$

At $T = T_N$, the magnetization becomes zero at each sublattice as in the case of a ferromagnet at $T = T_C$. T_N can be expressed by

$$T_N = \frac{ng^2 \mu_0 \mu_B^2 J(J+1)}{2k_B \mu_0} \tag{2.3.35}$$

or

$$T_N = \frac{\lambda C}{2\mu_0} \tag{2.3.36}$$

where C is the Curie constant as before.

For $T > T_N$, the magnetization depends on the applied external field B_0 such that the effective field on each sublattice is given by

$$\boldsymbol{B}_{eff}^{A} = \boldsymbol{B}_0 + \boldsymbol{B}_{in}^{A} = \boldsymbol{B}_0 - \lambda_2 \boldsymbol{M}_A - \lambda_1 \boldsymbol{M}_B \tag{2.3.37}$$

22

and

$$\boldsymbol{B}^B_{eff} = \boldsymbol{B}_0 + \boldsymbol{B}^B_{in} = \boldsymbol{B}_0 - \lambda_1 \boldsymbol{M}_A - \lambda_2 \boldsymbol{M}_B \qquad (2.3.38)$$

respectively. The susceptibility of an antiferromagnet can be shown to obey the Curie-Weiss law

$$\chi = \frac{C}{T - \theta_p} \qquad (2.3.39)$$

where θ_p is now expressed by

$$\theta_p = \frac{C(\lambda_1 + \lambda_2)}{2\mu_0}. \qquad (2.3.40)$$

θ_p is related to the Néel temperature by

$$\theta_p = \frac{\lambda_1 + \lambda_2}{\lambda_1 - \lambda_2} T_N. \qquad (2.3.41)$$

For $T < T_N$, the magnetization depends critically on the direction in which the magnetic field is applied with respect to the orientation of the magnetic moments. The field can be applied parallel or perpendicular to the magnetic moments with the corresponding $\chi_\parallel$ and $\chi_\perp$ susceptibilities. In poly-crystalline or powdered samples the average total susceptibility below T_N is given by [17]

$$\chi = \frac{1}{3}\chi_\parallel + \frac{2}{3}\chi_\perp. \qquad (2.3.42)$$

2.3.4 Ferrimagnetism

This is the behavior that is typically found in ferrite materials. The arrangement of magnetic moments is similar to that of an antiferromagnet. The two antiparallel aligned moments on the sublattices have unequal magnitude. This results in a non-zero net magnetization. The arrangement of magnetic moments is shown in Figure 2.8. Ferrimagnetism occurs in most oxides and is known to be an intermediate magnetic state between ferromagnetism and antiferromagnetism [39]. The net saturation magnetization can be modeled by

$$M = M_A - (1 - \lambda)M_B \qquad (2.3.43)$$

where $M_A \neq M_B$. When $M_A = M_B$ we can define the ferromagnetic state corresponding to $\lambda = 0$ or 1 and antiferromagnetic state for $\lambda = \frac{1}{2}$. The ferrimagnetic
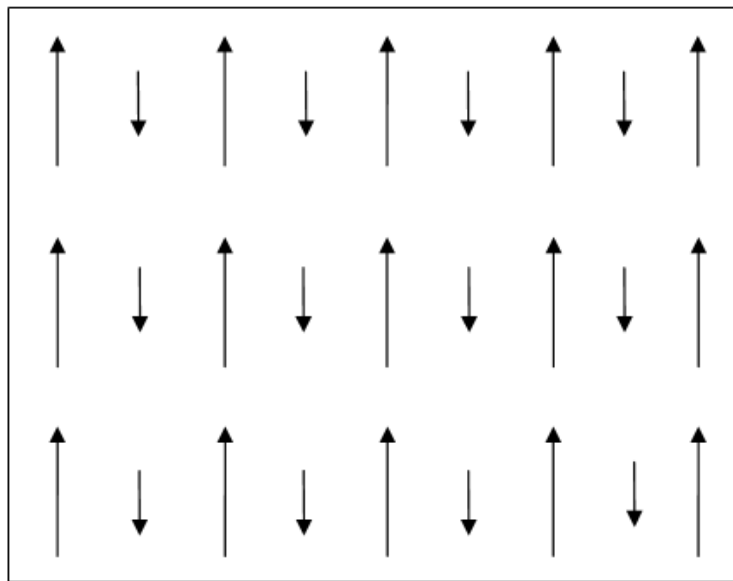
Figure 2.8: Alignment of magnetic moments in a ferrimagnetic material [37].

state occurs when $\lambda \neq 0, \frac{1}{2}$ or 1. In ferrimagnets, the net magnetization is always non-zero for $T < T_C$ except in the special case when the magnetizations of the two sublattices cancel out at $T_{comp} < T_C$ as shown in Figure 2.9. T_{comp} is known as the compensation temperature.

Above T_C, paramagnetic behavior is observed and the magnetization thus depends on the applied field. The magnetization at each sublattice is given by

$$\boldsymbol{M}_A = (C_A/T)(n_{AA}\boldsymbol{M}_A + n_{AB}\boldsymbol{M}_B + \boldsymbol{B}_0) \qquad (2.3.44)$$

and

$$\boldsymbol{M}_B = (C_B/T)(n_{AB}\boldsymbol{M}_A + n_{BB}\boldsymbol{M}_B + \boldsymbol{B}_0) \qquad (2.3.45)$$

where n_{AA}, n_{BB} and n_{AB} are the Weiss coefficients representing the intersublattice and intrasublattice interactions. The coefficient $n_{AB} < 0$ is regarded as an essential parameter representing strong negative exchange interactions. The Curie temperature for a ferrimagnet can be expressed by [17]

$$T_C = \frac{1}{2}\left[(C_A n_{AA} + C_B n_{BB}) + \sqrt{(C_A n_{AA} - C_B n_{BB})^2 + 4C_A C_B n_{AB}^2}\right]. \qquad (2.3.46)$$

The variation of the inverse susceptibility with temperature is shown in curve (b) in Figure 2.2 which can be expressed by

$$\frac{1}{\chi} = \left[\frac{T - \theta_p}{C_A + C_B} - \frac{C'}{T - \theta'}\right] \qquad (2.3.47)$$

where C_A, C_B, C' and θ' are the microscopic parameters of the material.

2.3.5   Superparamagnetism

Superparamagnetism occurs below the Curie temperature in nanosized ferromagnetic or ferrimagnetic materials. The nanoparticles are composed of single magnetic domains which are aligned in a ferromagnetic pattern. Thermal fluctuations of the moments exist on a microscopic level and some energy (ΔE) is required to overcome the crystal field anisotropy. In this case the magnetic moments has two stable antiparallel orientation separated by ΔE which is given by

$$\Delta E = KV\sin^2\theta \qquad (2.3.48)$$

25
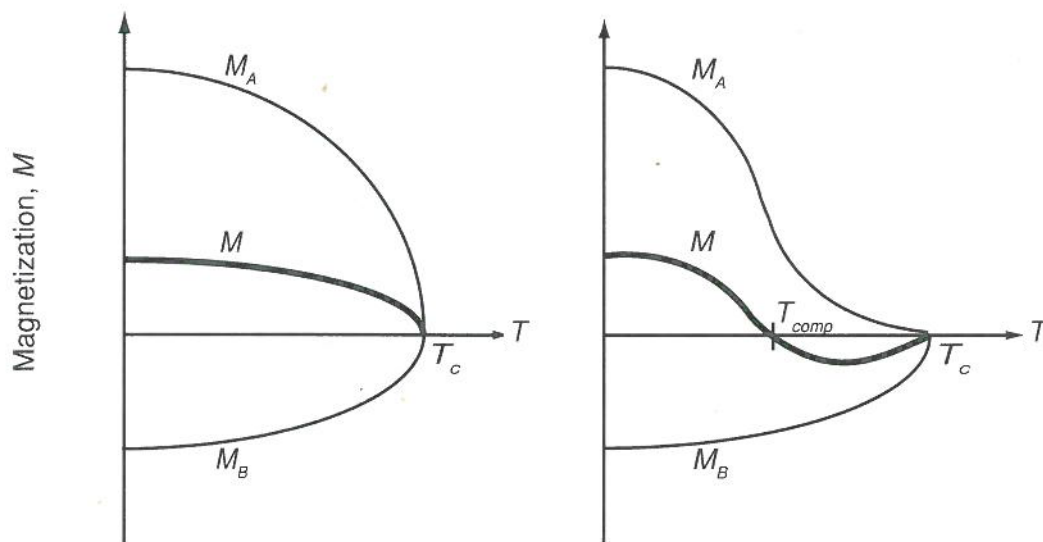
Figure 2.9: Sublattice magnetization, net magnetization and collapse of spontaneous magnetization at T_C and T_{comp} for a ferrimagnet [17].

where V is the volume of the nanoparticle, K is the effective uniaxial anisotropy energy density and θ is the angle between the direction of the moments and the easy axis. At $T_B < T < T_C$, there is a finite probability for the magnetization to flip its direction. The mean time between two flips is known as the Néel relaxation time (τ_N) and can be expressed by

$$\tau_N = \tau_m \exp\left(\frac{KV}{K_B T}\right) \tag{2.3.49}$$

where τ_m is the measuring time. For $\tau_m >> \tau_N$, a superparamagnetic state exists since the magnetization will flip several times thus resulting in an average measured magnetization of zero. The nanoparticles are said to be blocked for $\tau_m << \tau_N$ since no flips in magnetization are observed. The transition between the two states occurs when $\tau_m = \tau_N$ [40]. It is practical to observe the transition between the two states as a function of temperature such that

$$T_B = \left(\frac{KV}{\ln\left(\frac{\tau_N}{\tau_m}\right)}\right) \tag{2.3.50}$$

where τ_m is fixed. Below T_B, the nanoparticles are completely blocked and above T_B but less than T_C the nanoparticles are in a superparamagnetic state. This means that superparamagnetism can be destroyed by cooling. Experiments have also shown that T_B increases with crystallite sizes. When studying the magnetization as a function of applied field in the superparamagnetic range ($T_B < T < T_C$), it is observed that superparamagnets do not show hysteresis. The magnetization of a superparamagnet under the influence of magnetic field and temperature is described by the classical Langevin function [41]. The reduced magnetization in this case is given by

$$\frac{M(T)}{M_S(0)} = \coth x - \frac{1}{x} \tag{2.3.51}$$

where

$$x = \frac{\mu B_0}{k_B T} \tag{2.3.52}$$

and μ is the magnetic moment of single a domain particles. Superparamagnetic order can be confirmed by universal plots of reduced magnetization as a function of B_0/T in the temperature range $T_B < T < T_C$. Below T_B we expect the reduced

magnetization of nanoparticles to vary as [17]

$$\frac{M(T)}{M_S(0)} \approx \left(1 - \frac{k_B T}{2KV}\right).$$

(2.3.53)

2.3.6   Other types of magnetic order

Other types of magnetic order which are not discussed in the current work do exist in solids. Most are derivatives of the basic magnetic orders already discussed. Diamagnetism is one of the five basic magnetic orders found in solids. The other magnetic orders are incipient ferromagnetism, metamagnetism, speromagnetism, asperomagnetism, ideal spin glass, helimagnetism, mictomagnetism (cluster glass) and sperimagnetism (canted ferrimagnetism) [40].

2.4   Magnetic interactions

There are two types of magnetic interactions between magnetic moments namely dipole-dipole and exchange interactions. The dipole-dipole interaction can be shown to be too small to account for the observed magnetic order in solids. The origin of magnetic order is now known to be due to exchange interactions which have Quantum Mechanical origin. Two types of exchange interactions are known called direct and indirect exchange interactions. Direct exchange interactions give strong but short range coupling between magnetic moments that are close enough that their wavefunctions overlap. This interaction between magnetic moments with spins $\boldsymbol{S}_i$ and $\boldsymbol{S}_j$ is expressed by the Heisenberg hamiltonian

$$H_e = -J_{ij}\boldsymbol{S}_i.\boldsymbol{S}_j.$$

(2.4.1)

The parameter J_{ij} is called the exchange integral [6]. The magnitude of J_{ij} depends on the interatomic distance. J_{ij} can be positive or negative depending on the balance of the Coulomb and kinetic energies [42]. The exchange integral (J_{ij}) is positive for parallel aligned spins (ferromagnets) and negative for antiparallel aligned spins (antiferromagnets). Magnetic moments over relatively large distances can also interact through an intermediary. This is called indirect exchange interaction. In metals, the conduction electrons can act as intermediaries. In this case the interaction is

called RKKY interaction named after Ruderman, Kittel, Kasuya and Yoshida [42]. When distant magnetic moments interact through a non-magnetic ion, the indirect exchange interaction is called superexchange interaction. In ferrites, the interaction between magnetic moments occurs via non-magnetic oxygen ions.

2.5   Magnetization process

The magnetization process can be explained by rotation of magnetization or by displacement of domain walls. The external influences and internal microstructure play a vital role in the magnetization process of a material. In rotational magnetization we assume that the magnetic field is applied at an angle θ_0 from the direction of the uniaxial magnetic flux as shown in Figure 2.10. The energy per unit volume of the system is given by

$$E = K \sin^2 \theta - \mu_0 M_S H \cos(\theta_0 - \theta) \tag{2.5.1}$$

where K is the magnetic uniaxial anisotropy constant [43]. We assume that a magnetically ordered material is constituted of domains and domain walls. In the presence of external fields the magnetization is uniform in the domains and non-uniform in the domain walls. The magnetization process can be demonstrated by performing isothermal measurements of magnetization as a function of applied magnetic field. The results are presented in the form of a hysteresis loop as shown in Figure 2.11. The saturation magnetization is approached at high fields through irreversible domain wall movements and rotations of individual magnetic moments [6]. The saturation magnetization can be approximated by an empirical relationship of the form

$$M(H) = M_s(0) \left(1 - \frac{a}{H} - \frac{b}{H^2} - .... \right) + \chi H \tag{2.5.2}$$

where a and b are fit parameters and χ is the high-field susceptibility [39]. Residual magnetism known as remanence M_R remains in the material after reducing the field back to zero. The coercive force H_C is the reverse magnetic field required to reduce the remanence to zero. The hysteresis loop provides information about the domain wall movements. The bigger the coercive fields the harder it is to reverse the magnetization. Hence the hysteresis loop can distinguish between soft and hard
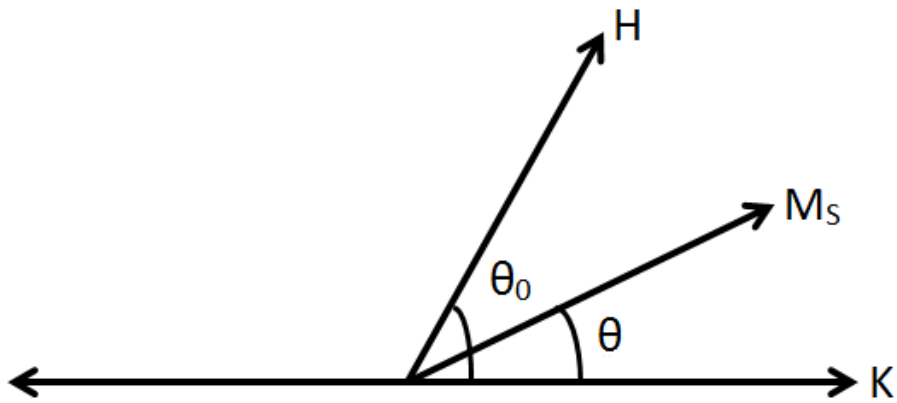
Figure 2.10: Rotation of magnetization from easy axis [43].
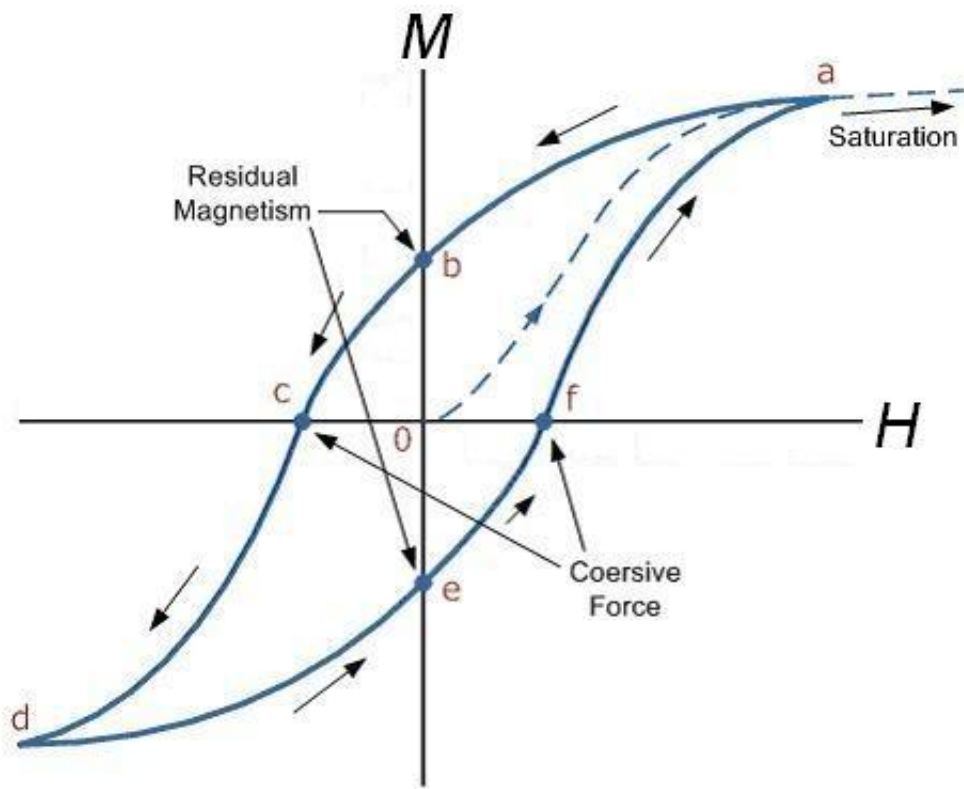
Figure 2.11: Isothermal variation of magnetization with applied magnetic field in a ferromagnet [44].

magnets. From the magnetization measurements we can determine the Curie points of materials and also deduce information about critical exponents in the vicinity of T_C.

Chapter 3

Experimental techniques

3.1   Introduction

The magnetic properties of spinel nanoparticles are strongly dependent on the ions involved and their distribution in the tetrahedral (A) and octahedral (B) interstitial sites [6]. All the important factors contributing to the variation of magnetic properties of these ferrites such as the grain size, morphology, crystallinity and cation distribution are strongly influenced by the preparation methods [45]. Since this is the case, a variety of synthesis methods are used to control and change these factors. The synthesis techniques include hydrothermal, glycol-thermal, co-precipitation, sol-gel and high-energy ball milling techniques [46]. In this study we have chosen to synthesize our samples by the glycol-thermal technique because of its ability to produce single phase materials at low synthesis temperature. The high-energy ball milling technique has been used to complex tetracycline-HCl with a $Mg_{0.5}Zn_{0.5}Fe_2O_4$ sample. The non-equilibrium nature of the milling process also allows for the preparation of nanoferrite powders with improved and novel properties [46]. X-ray diffraction (XRD) was used to confirm single phase formation and to estimate crystallite sizes. The samples were further subjected to Mössbauer spectroscopy and magnetization measurements at room temperature ($\simeq$ 300 K).

3.2 Glycol-thermal technique

This is a wet chemistry technique in which metal chloride or nitrate salts are used as starting materials to produce a desired composition of the product material. The stoichiometric values of the reactants are measured and mixed in deionised water to form a solution. A wet homogeneous precipitate of the reactants is formed by adding ammonium hydroxide to chloride solutions or by adding sodium hydroxide or potassium hydroxide to nitrate solutions. Usually the precipitates are washed by deionised water in order to remove the chloride and alkali ions before further processing. The precipitate is then heated in ethylene glycol in a high pressure vessel under continuous stirring for sufficient time to allow the reaction to take place. The reaction temperature and reaction time play a crucial role in obtaining single phase samples. Our sample syntheses were performed by using the PARR 4843 stirred pressure reactor shown in Figure 3.1. The pressure reactor consists of a reaction chamber and a controller. The reaction chamber is equipped with a high temperature heater, stirrer, pressure gauge and a temperature sensor. The controller monitors continuously the reaction conditions. Figure 3.2 shows the operation schedule of the reactor in the synthesis of all our samples.

In the present work we have synthesized a series of $Mg_{1-x}Zn_xFe_2O_4$ nanoferrites (for $0 \leq x \leq 1$). High purity metal chlorides salts were used in the synthesis of the compounds. The starting materials were $MgCl_2.6H_2O$ (99.0%), $ZnCl_2$ (99.999%) both supplied by Sigma Aldrich and $FeCl_3.6H_2O$ (99%) which was supplied by Merck Chemicals (Pty) Ltd. Stoichiometric amounts of the starting materials were used in order to produce the targeted compositions of 3 g about per sample. The chlorides were mixed together in 400 ml of deionised water using a magnetic stirrer for about 30 minutes or until all the salts had completely dissolved. Ammonium hydroxide solution (NH_4OH) was slowly added to the solution until full precipitation was achieved at a pH value of about 9.5. The precipitated solutions were poured into four 50 ml falcons (Conical Centrifuge Tubes) which we secured to the falcon adapters.
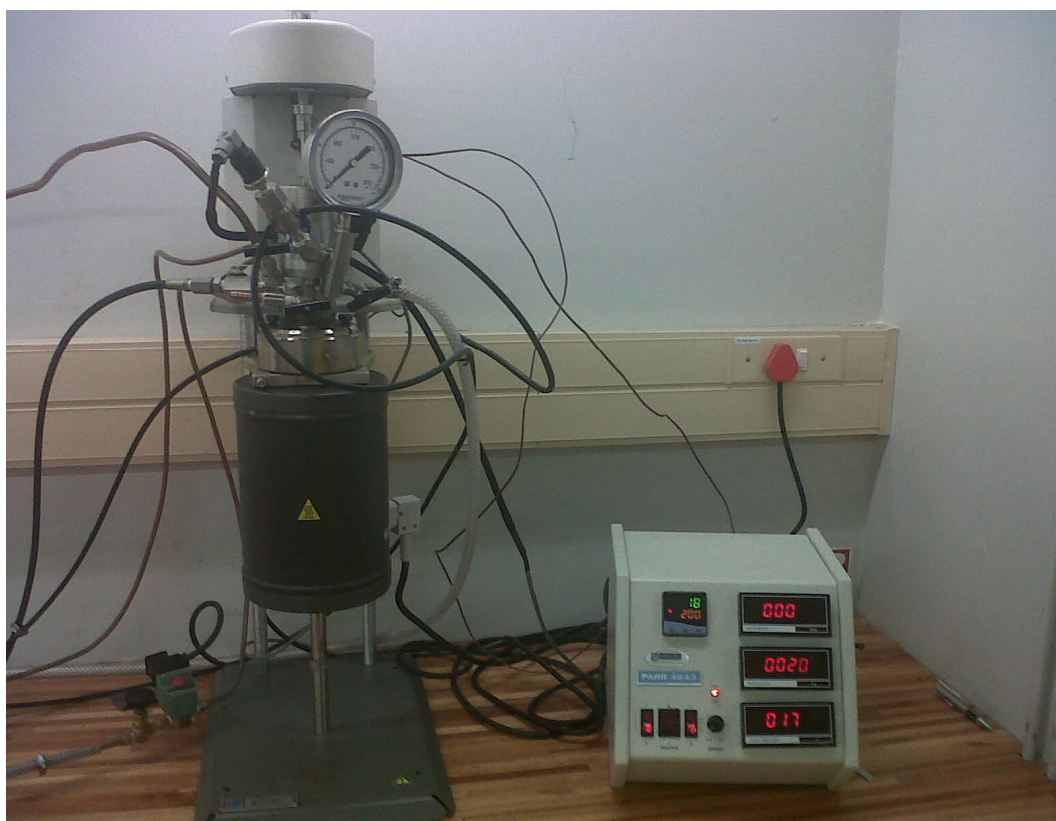
Figure 3.1: The PARR 4843 stirred pressure reactor.
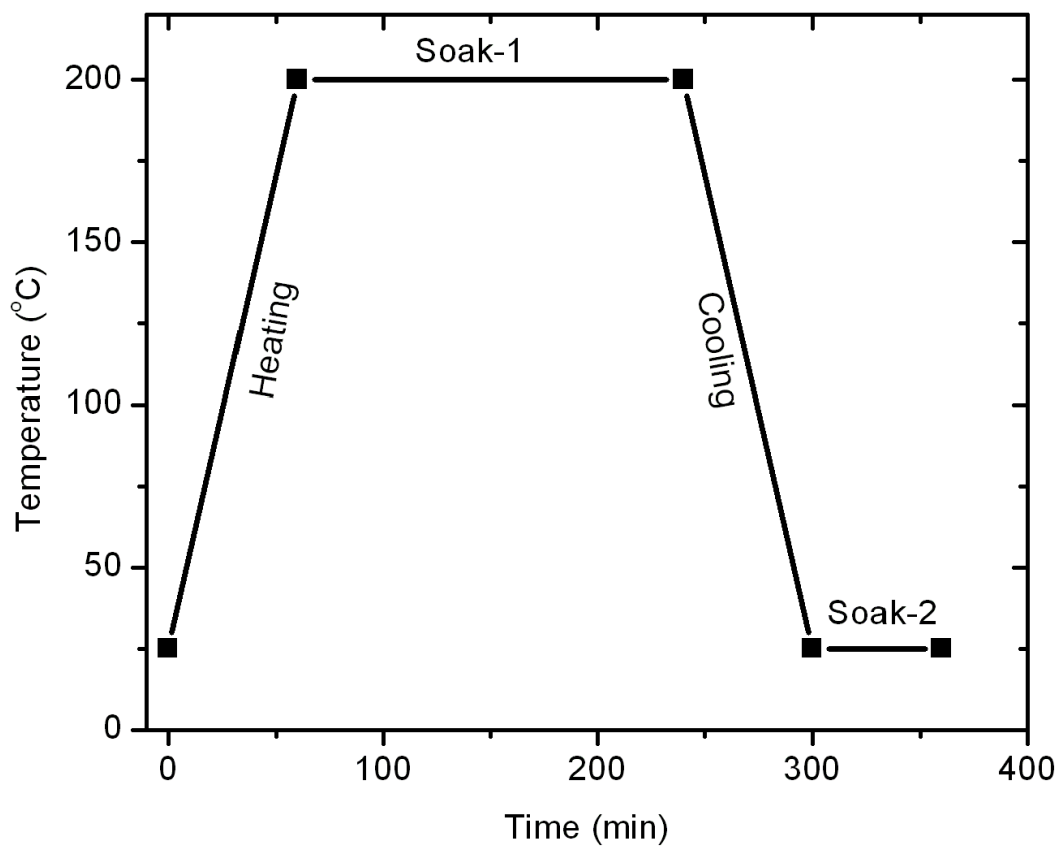
Figure 3.2: The operation schedule of the PARR 4843 pressure reactor.

The four adapters with the falcons were then placed into the stations of an Eppendorf Centrifuge model 5207 shown in Figure 3.3. Figure 3.4 shows the uncentrifuged precipitate solutions which have unwanted chlorides. The precipitate solutions and subsequent dilutions by dionised water were then centrifuged at 1500 relative centrifugal force (rcf) for two minutes to allow for the precipitate to settle at the bottom of the tubes as shown in Figure 3.5. The clear solution was poured in a glass beaker and tested for the presence of chloride ions by adding a standard solution of $AgNO_3$. This was repeated several times until no chloride ions were detectable. About 250 ml of ethylene glycol was used as the reaction medium for the precipitate in the pressure reactor which was operated at 200 °C under rapid stirring at 300 rpm for 3 hours. For all our samples, the pressure in the reactor vessel varied between 120 and 130 psi. The sample was removed from the pressure vessel and centrifuged at 2000 rcf for 4 minutes as it took longer time to sediment the precipitate after the heat treatment. This allowed the removal of the ethylene glycol. The precipitate was briefly washed as above by deionised water and finally by 200 ml of ethanol in order to aid the drying process of the sample. The synthesized compounds were dried for 6 hours in a vacuum flask under a 200 W infrared light. The final products were homogenized and ground to fine powder by a mortar and pestle in readiness for further measurements and processing.

3.3 High-energy ball milling

High energy ball milling is a multi-purpose technique that can be used to synthesize compounds and to complex powders uniformly. Milling can also be used to reduce particle sizes of bulk materials to nanosize [6]. When synthesizing compounds, metal oxides or carbonates can be used as starting materials to produce the desired composition of the final product. For the purposes of this study, we have used high-energy ball milling to complex Tetracycline-HCl with $Mg_{0.5}Zn_{0.5}Fe_2O_4$ nanoferrite. The required molar ratio of the reactants is chosen and then used with individual molecular masses of the reactants and the product to calculate the correct mass for each reactant. The ball-to-sample mass ratio is chosen in advance in order to

Figure 3.3: Eppendorf centrifuge used to remove excess chlorides during the synthesis of $Mg_{1-x}Zn_xFe_2O_4$ nanoparticles.

Figure 3.4: Uncentrifuged precipitate of $Mg_{1-x}Zn_xFe_2O_4$ samples.

Figure 3.5: Centrifuged precipitate of $Mg_{1-x}Zn_xFe_2O_4$ samples.

determine the number of balls needed for a particular sample size m_s. The number of balls n_b required in each grinding jar can be calculated from the equation

$$n_b = \frac{r_{bs}m_s}{m_b} \tag{3.3.1}$$

where r_{bs} is the ball-to-sample mass ratio and m_b is the average mass of the balls. The starting materials were pre-mixed and sealed in grinding steel jars with an appropriate number of balls.

The complexing of the Tet-NF was carried out on a Retsch PM 400 planetary ball mill MA type shown in Figure 3.6. This instrument has four workstations which allow the milling of four different samples at the same time. It also has an on-board controller which allows the setting of the milling time interval, speed and mode. The user can choose one out of the two modes of milling depending on the way the samples are to be milled. The first mode rotates the workstations continuously in a clockwise direction. In the second mode the workstations alternate in rotation between clockwise and anticlockwise directions at pre-set time intervals. The later is the mode of rotation used in the complexing of our samples. The grinding was performed in 250 ml hardened steel jars in air and argon atmospheres using steel balls.

The $Mg_{0.5}Zn_{0.5}Fe_2O_4$ composition with equal proportions of Zn and Mg was chosen to be the best representative compound sample to complex with Tetracycline-HCl in order to form the Tet-NF complexes. Zinc and magnesium are both essential elements in the human body and are non-toxic. We have used a 1:1 molar ratio of the reactants (1.6 g of $Mg_{0.5}Zn_{0.5}Fe_2O_4$ and 3.489 g of Tetracycline-HCl) to produce about 5 g of the Tet-NF complex in each grinding jar. The ball to sample ratio was chosen to be 20:1. The samples were pre-mixed and sealed with 16 steel balls in each jar. The mass of each ball was 4.05 g. The two grinding jars with air and argon environments were placed and secured on opposite workstations of the planetary ball mill in order to balance the rotations during the milling process. The complexes were milled for 1, 3, 5, 15 and 30 hours at 200 revolutions per minute (rpm). About 0.5 g of sample was removed from each jar for characterization after each milling interval.

Figure 3.6: Retsch PM 400 high-energy planetary ball mill used for the complexing of Tetracycline-HCl with $Mg_{0.5}Zn_{0.5}Fe_2O_4$.

3.4 X-ray diffraction

X-ray diffraction (XRD) is a characterization technique that is widely used to determine the structural properties of materials. XRD is based on the interaction of X-rays with crystalline substances which generate XRD patterns which are characteristics of the structure of the material. An XRD pattern is therefore regarded as a fingerprint of that particular substance [47]. Ferrites reported in this study have the spinel structure. In this regard, the single phase formation is confirmed by indexing all the primary peaks in the diffraction pattern with respect to the known Miller indices of the cubic spinel structure. XRD is governed by Bragg's law

$$n\lambda = 2d\sin\theta \tag{3.4.1}$$

where n is an integer related to the order of the diffraction, λ is the X-ray wavelength, d is the perpendicular distance between lattice planes and θ is the angle of incidence of X-rays with the lattice plane which is also known as the Bragg's angle [48]. Figure 3.7 shows the graphical representation of Bragg-scattering. For a cubic spinel structure, the lattice parameter a define the size of the unit cell in a crystal lattice which is related to the d-spacing by the formula

$$a = d\sqrt{h^2 + k^2 + l^2} \tag{3.4.2}$$

where h, k and l are the corresponding Miller indices for the diffracting planes [33]. The lattice parameter can be easily determined by combining equation (3.4.1) and equation (3.4.2) to give

$$a = \frac{n\lambda\sqrt{h^2 + k^2 + l^2}}{2\sin\theta}. \tag{3.4.3}$$

The crystallite size D and the crystallite XRD density ρ_{xrd} are important parameters which can be determined from XRD pattern analysis. The peak broadening of the most intense (311) peak can be used to estimate the crystallite sizes by the Scherrer formula

$$D = \frac{K\lambda}{\beta\cos\theta} \tag{3.4.4}$$

where K is a constant dependent on crystalline shape, λ is the X-ray wavelength, β is the full width at half maximum (FWHM) of the peak and θ is the Bragg angle [49]. K is approximately 0.9 for the cubic spinel structure [50].
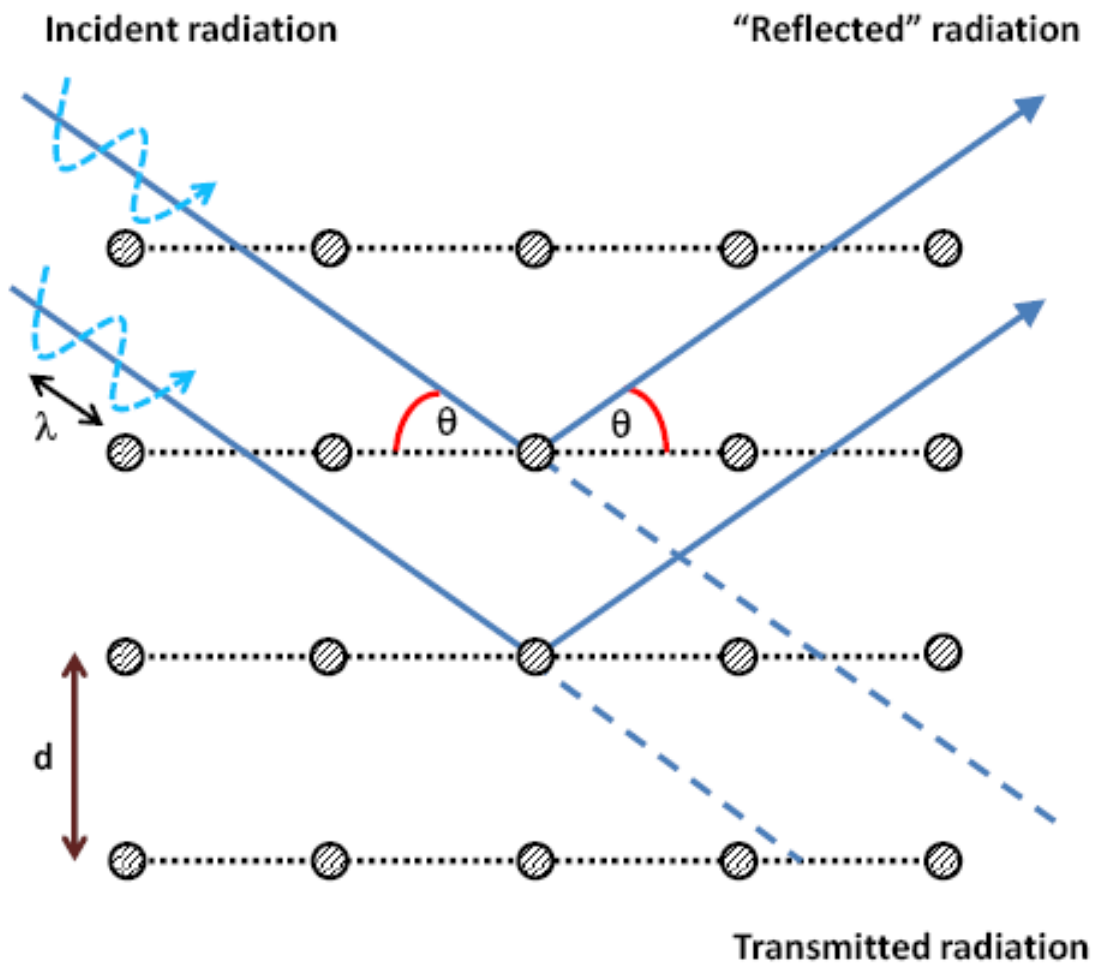
Figure 3.7: Graphical representation of Bragg-scattering [47].

Density plays an important role in controlling the properties of polycrystalline ferrites [3]. The XRD density (ρ_{xrd}) gives information about the packing of atoms in a unit cell. In cubic spinels

$$\rho_{xrd} = \frac{8M}{N_A a^3} \qquad (3.4.5)$$

where 8 refers to the number of molecules per unit, M is the molecular weight, N_A is the Avogadro's number and a is the size of the lattice constant which defines the size of the unit cell [51]. Figure 3.8 shows the Bruke D8 ADVANCE diffractometer which we used to perform the XRD measurements.

Other parameters relating to the packing of atoms in a material not reported in this study are the bulk density ρ_b and porosity P. If enough sample is available, ρ_b can be obtained by making pellets. Once the dimensions of the pellet are known, ρ_b can be calculated using the formula

$$\rho_b = \frac{m}{\pi r^2 t} \qquad (3.4.6)$$

where m is the mass, r is the radius and t is the thickness of the pellet. The volume of the pellet is given by $\pi r^2 t$. The porosity is defined as a percentage which gives information about the amount of empty spaces in between crystallites. This is defined as

$$P = (1 - \frac{\rho_b}{\rho_{xrd}})100. \qquad (3.4.7)$$

The smaller the value of P, the larger the crystallite sizes.

3.5   Mössbauer spectroscopy

Mössbauer spectroscopy is a technique that is used to study materials because of its ability to detect the weak interactions between a nucleus and its surroundings. Scientists use the tiny energy changes to give precise information about the chemical, structural and magnetic properties of materials. Geologist use this technique in mineralogy to examine the valence states of iron atoms at lattice and interstitial sites. The technique is important for both research and applications. In 1957 Rudolf Mössbauer discovered the recoil-free emission and resonant absorption of gamma (γ)

Figure 3.8: Bruker D8 ADVANCE diffractometer used for XRD measurements.

rays by atoms in a crystal. This is known as the Mössbauer effect and serves as a basis for Mössbauer spectroscopy.

3.5.1 Mössbauer effect

The Mössbauer effect is a recoilless emission of γ-ray photons by an emitter nucleus and resonant absorption of those γ-rays by an identical nucleus in the absorber material without thermal broadening [52, 53]. For our ferrite samples, the identical nuclei in the source and absorber material are ^{57}Fe isotopes. The natural abundance of ^{57}Fe isotope in a material containing Fe atoms is 2.12% [17]. Figure 3.9 shows a graphical representation of resonant absorption. Some conditions must be satisfied in order for resonant absorption of photons to occur. The transition energy (E_T) of the identical emitter and the absorber nuclei is given by

$$E_{es} - E_{gs} = E_T = E'_{es} - E'_{gs}.$$ (3.5.1)

The energy levels are defined in Figure 3.9. In recoilless emission, all the transition energy is transferred to the gamma ray such that

$$E_T = E_\gamma$$ (3.5.2)

for the resonant absorption to occur. However, recoilless emission and absorption of γ-rays is in conflict with conservation of energy and momentum and is thus impossible for free atoms. Figure 3.10 shows an illustration of the recoil energy due to conservation of momentum as a nucleus emits or absorbs a γ-ray photon. The recoil energy during the absorption or emission of γ-ray photon by a nucleus of mass M can be shown to be

$$E_R = \frac{E_\gamma^2}{2Mc^2}$$ (3.5.3)

where c is the speed of light [54]. The uncertainty in energy corresponds to the linewidth Γ of the γ-ray whilst the uncertainty in time corresponds to the mean-life τ of the nuclear state [54]. The two parameters are related through the Heisenberg relation by

$$\Gamma = \frac{\hbar}{\tau}$$ (3.5.4)
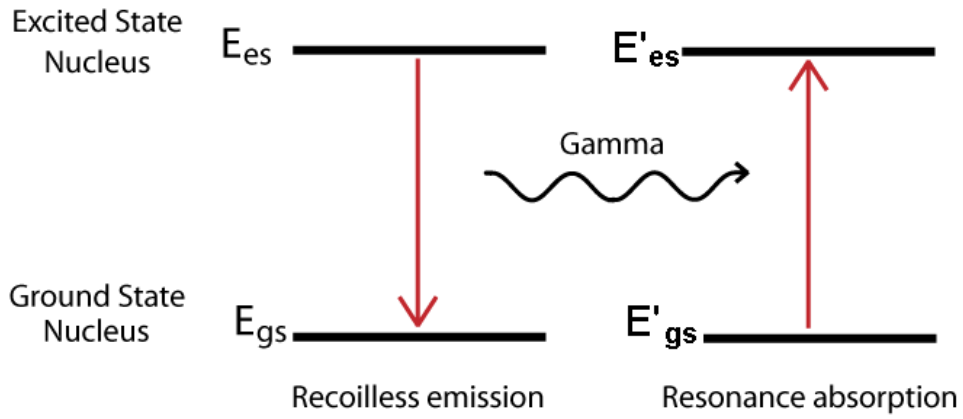
Figure 3.9: Graphical representation of resonant absorption [55].

Figure 3.10: The excited nucleus on the left hand side (LHS) emits a γ-ray photon to the right hand side (RHS) and recoils to the LHS (emission). A nucleus in the ground state on the RHS absorbs the γ-ray photon on the LHS and recoils to the RHS (absorption) [56].

where $\hbar$ is the Planck's constant. For nuclear transitions, resonant absorption does not occur when

$$E_R > \Gamma. \tag{3.5.5}$$

To limit the energy loss by recoil, we can consider the emitting and absorbing nuclei to be fixed in a solid matrix. The recoil will then be shared by the whole crystal. This makes the mass M in equation (3.5.3) to be much larger and thus making the recoil energy $E_R \approx 0$ and $E_T \simeq E_\gamma$. This would satisfy the condition for resonant absorption. Another way to achieve resonant condition is to Doppler shift the γ-ray energy by vibrating the source or emitter nucleus. This is a common method of achieving resonant absorption during Mössbauer spectroscopy experiments. The γ-ray energy is Doppler shifted by a factor

$$\delta E = E_\gamma \frac{v}{c} \tag{3.5.6}$$

where v is the velocity of the vibrating source in a few mm/s [53]. In our set-up, a 25 mCi ^{57}Co source sealed in Rh matrix and vibrated at constant acceleration was used as a source of γ-rays. Figure 3.11 shows the schematic decay of ^{57}Co to produce ^{57}Fe nuclei. The Mössbauer spectroscopy measurements are based on the emission and absorption of the 14.41 keV γ-ray. The experimental data consist of the transmitted intensities through the absorber as a function of the Doppler velocity. Using suitable Mössbauer analysis software such as Recoil, Mosswinn and NORMOS electrostatic and magnetic information can be deduced from the spectra. The Recoil Mössbauer analysis software has been used to analyse all the spectra in the present work. In the next section we discuss the different types of interactions in absorber materials that can be deduced using Mössbauer spectroscopy.
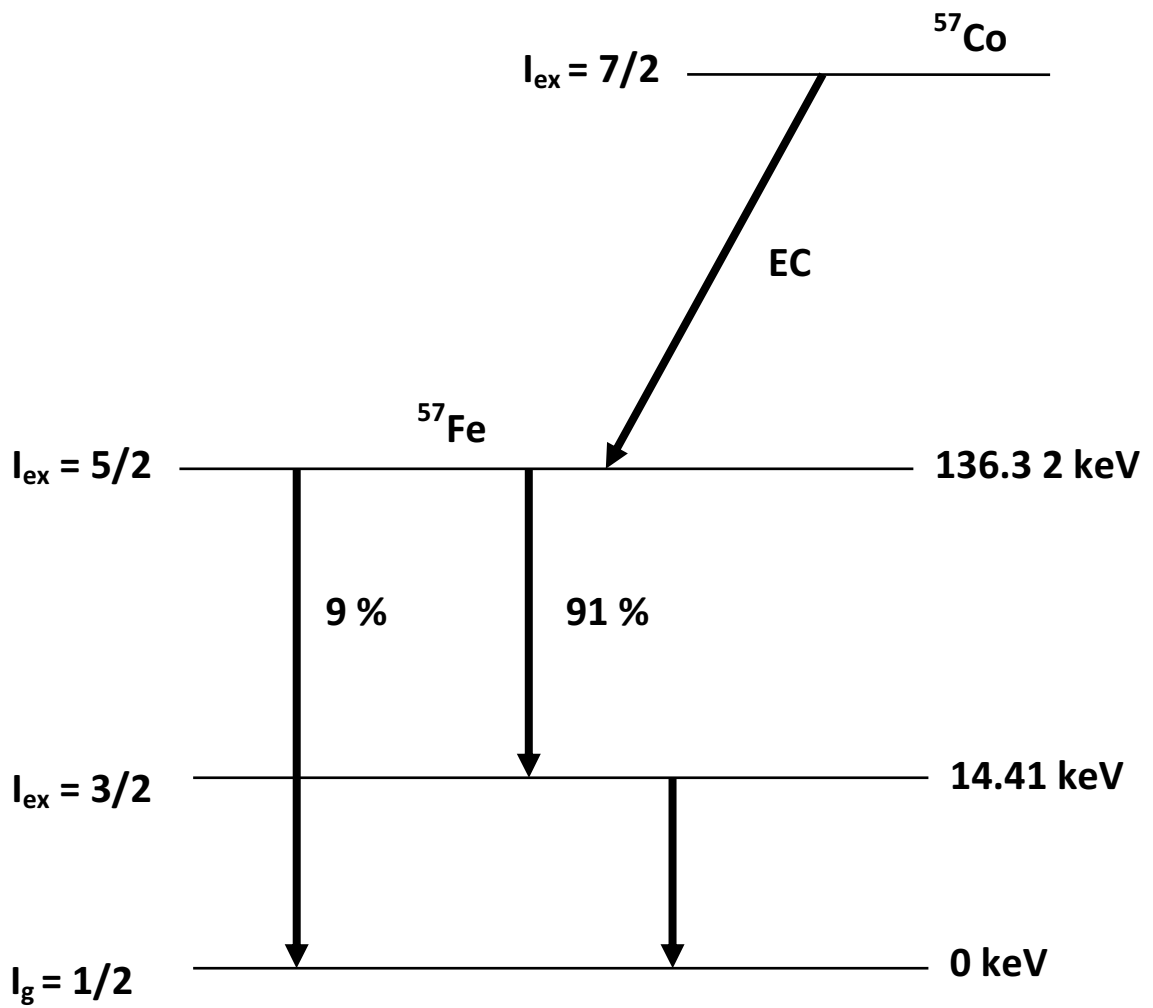
Figure 3.11: Schematic diagram showing the nuclear decay of ^{57}Co to produce ^{57}Fe nuclei [57].

3.5.2 Hyperfine interactions

Electrostatic and magnetic interactions between the nucleus and its environment are collectively known as hyperfine interactions. These interactions results in the small splitting of the nuclear energy levels which are used for characterization of materials. These include the chemical isomer shift δ, electric quadrupole interaction Δ and magnetic hyperfine interaction H. The effects of δ, Δ and H on the nuclear energy levels is illustrated in Figure 3.12 [58]. Further details of the origin and impact of each of the interactions are given in the following sub-sections.

3.5.2.1 Chemical isomer shift

Isomer shift or chemical shift is a shift in resonance energy due to the difference in the s-orbital electron density between the source and the absorber nuclei. It is dependent on the difference of the nuclear radii of the ground and excited states of the source and absorber [54]. However, the screening effects give the p, d and f-electrons an influence on the s-electron density. The s-electron density is known to be affected by the oxidation state of the atom. Hence, during Mössbauer spectra analysis, the oxidation state of the atom can be deduced from the isomer shift value [59]. This has been proven by the different isomer shift values for Fe^{2+} and Fe^{3+} even though their atomic configuration differ by a d-electron which does not contribute to the charge density. The $3s$-electrons are further from the nucleus than the $3d$-electrons. The additional d-electron reduces the Coulomb potential and causes the wave function of the $3s$-electrons to expand. This results in reduced charge density and a greater net difference between the nuclear states for the source and absorber. The isomer shift is observed as a shift in the centroid of a Mössbauer spectra from the zero velocity center. The shift can be either to the right or left depending on the difference in the electron charge density. The isomer shift is actually the difference in the nuclear state between the source (S) and absorber (A) nuclei given by

$$\delta = E_A - E_S. \tag{3.5.7}$$

The approximate isomer shift value with Doppler velocity is given by

$$\delta = \frac{2\pi}{5} Ze^2 [|\psi_A(0)|^2 - |\psi_S(0)|^2][R_{ex}^2 - R_{gd}^2] \tag{3.5.8}$$
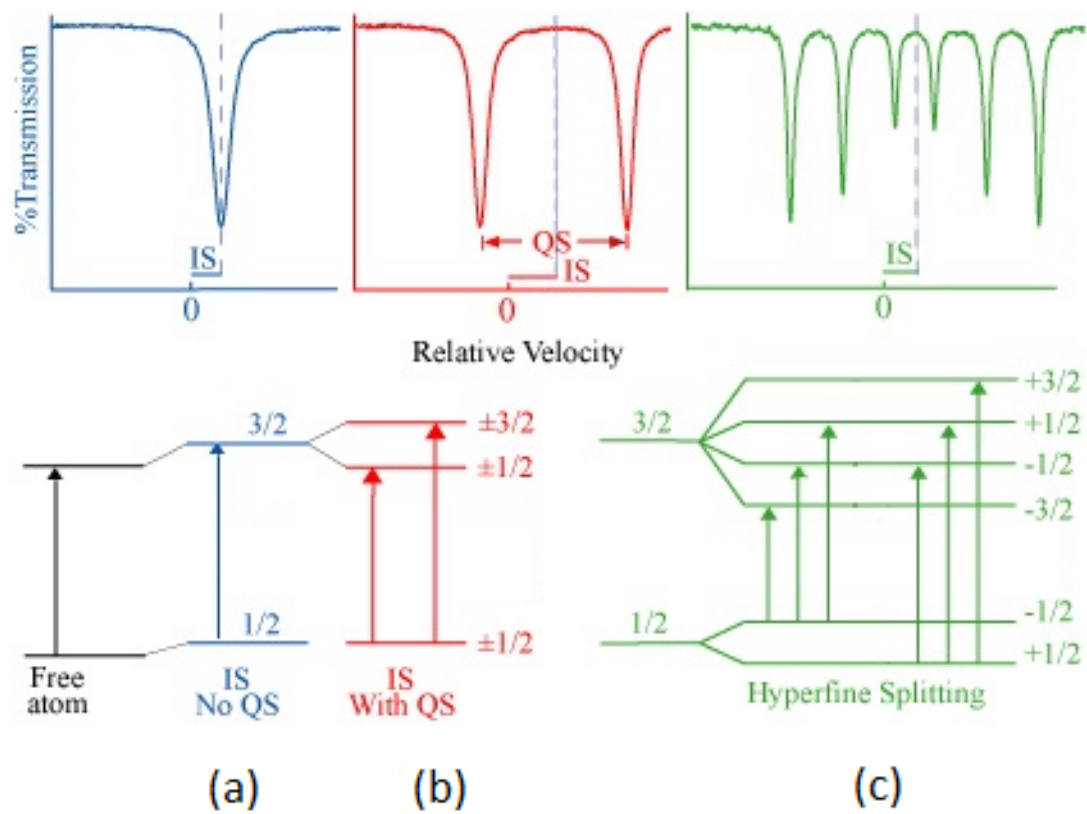
Figure 3.12: Shifts in nuclear energy levels resulting from chemical isomer shift (IS), electric quadrupole interaction (QS) and magnetic hyperfine interaction [58].

where Z is the atomic number, e is the electron charge, $|\psi_A(0)|^2$ and $|\psi_S(0)|^2$ are the s-electron densities of the absorber and source respectively. R_{ex} and R_{gd} are the radii of the excited and ground states respectively. In a Mössbauer spectrum, the isomer shift is given in velocity units (mm/s) where 1 mm/s is equivalent to 4.8×10^{-8} keV for ^{57}Fe isotope [53]. Calibrating the spectra helps in reporting the isomer shift with reference to the standard absorber. Alpha iron is commonly used as a standard absorber in ^{57}Fe Mössbauer spectroscopy.

3.5.2.2 Electric quadrupole interaction

The electric quadrupole interactions occur between the nuclear quadrupole moment and the electric field gradient (EFG) resulting in all or part of their $(2I+1)$-fold degeneracy to split. The quadrupole splitting is only observed in non-spherical nuclei where the nuclear quantum number $I > \frac{1}{2}$. The nuclear quadrupole moments arise from the splitting of the nuclear energy levels produced by an asymmetric electric field caused by non-spherical charge distribution. For nuclei with an excited state of $I_{ex} = \frac{3}{2}$ like ^{57}Fe and ^{119}Sn, the interactions split the excited state into two degenerate energy sub-levels corresponding to $m_I = \pm\frac{3}{2}$ and $m_I = \pm\frac{1}{2}$ [53]. This is well illustrated in Figure 3.12 (b). The γ-transitions occur between the states $m_I = \pm\frac{3}{2} \rightarrow \pm\frac{1}{2}$ and $\pm\frac{1}{2} \rightarrow \pm\frac{1}{2}$. These transitions are observed as two separate peaks in a Mössbauer spectrum referred to as a 'doublet'. The separation between the two peaks is called the quadrupole splitting Δ which is given by

$$\Delta = \frac{eV_{zz}Q}{2} \tag{3.5.9}$$

which reflects the electric field at the nucleus. V_{zz} is the electric field tensor and Q is the electric quadrupole moment. The quadrupole splitting is also quoted in mm/s.

3.5.2.3 Magnetic hyperfine interaction

Magnetic hyperfine interactions occurs because of the presence of a magnetic field at the nucleus. The magnetic field can be internal originating from the atoms themselves or external by placing the sample in an applied magnetic field. The nuclear magnetic dipole moment ($\boldsymbol{\mu}$) will tend to align itself with the field. The

interaction between $\boldsymbol{\mu}$ and magnetic field ($\boldsymbol{H}$) results in the magnetic splitting of energy levels also referred to as nuclear Zeeman splitting. The Hamiltonian describing the interaction is given by

$$H_e = -\boldsymbol{\mu.H} = -g\mu_N\boldsymbol{I.H} \qquad (3.5.10)$$

where μ_N is the the nuclear Bohr magneton and g is the nuclear gyromagnetic ratio also referred to as the g-factor [54]. The g-factor is given by

$$g = \frac{\mu}{I\mu_N} \qquad (3.5.11)$$

and μ_N has the value of $5.04929{\times}10^{-27}$ J T^{-1} [53]. The eigenvalues values of the above Hamiltonian are given by

$$E_m = -\frac{\mu H m_I}{I}. \qquad (3.5.12)$$

The magnetic field splits the energy levels into equally spaced $2I+1$ non-degenerate energy sub-levels. In the case of ^{57}Fe nuclei, the excited state $I_{ex} = \frac{3}{2}$ splits into four non-degenerate energy sub-levels corresponding to $m = -\frac{3}{2}, m = -\frac{1}{2}, m = \frac{1}{2}$ and $m = \frac{3}{2}$ as shown in Figure 3.12 (c). The ground state splits into two non-degenerate states corresponding to $m = \frac{1}{2}$ and $m = -\frac{1}{2}$. The γ-ray transitions occur between the different nuclear energy levels governed by the selection rule $\Delta m_I = 0, \pm 1$. There are six allowed γ-ray transitions in the order of $-\frac{3}{2} \rightarrow -\frac{1}{2}$, $-\frac{1}{2} \rightarrow -\frac{1}{2}$, $-\frac{1}{2} \rightarrow \frac{1}{2}$, $\frac{1}{2} \rightarrow -\frac{1}{2}$, $\frac{1}{2} \rightarrow \frac{1}{2}$ and $\frac{3}{2} \rightarrow \frac{1}{2}$. These γ-ray transitions are observed as six lines in a Mössbauer spectra as shown in Figure 3.12 usually referred to as a 'sextet'. The widths of the sextet lines are assumed to be the same. The ratio of the absorption peaks is given by 3:2:1:1:2:3 for a thin Fe-absorber [52].

3.5.3 Experimental set-up

The Mössbauer spectroscopy unit used for measurements consists of a 25 mCi ^{57}Co source sealed in rhodium matrix, HALDER D 8110 transducer, LND 45431 detector, FAST ComTec pre-amplifier, CANBERRA 2011 linear amplifier, TUNNELEC TC-950 HV supply, HALDER MR-351 Mössbauer drive unit (MDU), an ORTEC model MCS-PCI card and a desktop computer. Figure 3.13 shows a block diagram for the
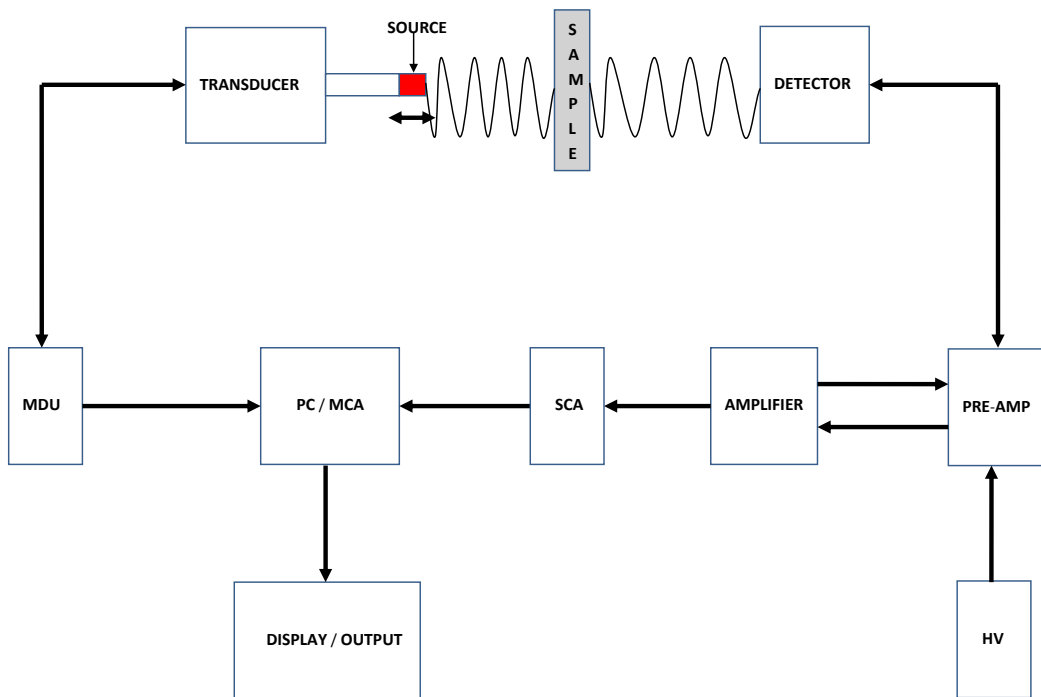
Figure 3.13: Graphical representation of Mössbauer spectroscopy experimental set-up shows the connection of the high voltage (HV) to the detector through the pre-amplifier.

Mössbauer spectrometer used for magnetic measurements in this study. The MDU is the most important component as it it gives the mode of vibration of the transducer and the constant acceleration rate to achieve resonant absorption. The amplified signal from the detector goes through a single channel analyser (SCA) then to the multi channel analyser card in the computer for data capturing. The captured data is displayed in form of a spectra using the MCS 32 Mössbauer computer program.The source, transducer and the detector were covered by 1 cm thick lead blocks to minimize exposure to radiation. The transducer was operated at 25 Hz and the velocity was varied in a range between 4 - 14 mm/s depending on whether the expected spectra was a doublet or a sextet. The spectra was calibrated by a standard α-iron (99.5 %) foil. The measurements were limited to the Mössbauer peak with γ-ray energy of 14.41 keV in order to observe the hyperfine interaction between the nucleus and its environment. At-least 1 million passes ($\simeq$ 24 hours recording time in MCS mode) were recorded for one spectrum to be ready for analysis.

3.6   Magnetization measurements

The magnetization is an important parameter to measure as it provides crucial intrinsic information about the magnetic state of a material and also gives information on the nature of the interactions of the constituent magnetic moments. The magnetization is well determined under the influence of an external magnetic field. The role played by the external field is to align the magnetic moments in the direction of the field. A vibrating sample magnetometer (VSM) shown in Figure 3.14 is commonly used to measure magnetization. One important aspect is to study how the magnetization of a material varies with temperature T or applied field B. Vibrating samples magnetometers are based on Faraday's law of induction. The principle of measurement is that if a sample is vibrated in sinusoidal motion in a uniform field, a sinusoidal electrical signals can be induced in suitably placed stationary pick-up coils [60]. The amplitude of the output signal is proportional to the magnetization of the sample being studied [61]. Our LakeShore VSM system consisted of an electromagnet, model 642 bipolar electromagnet power supply, model 450 gaussmeter,

Figure 3.14: Lakeshore 735 vibrating sample magnetometer used for magnetization measurements.

model 340 temperature controller, model 735 VSM controller, a NESLAB Ther-moFlex 2500 chiller, National Instruments IEEE-488 interface card and a desktop computer. The components were connected to the interface card by PCI-GPIB cables. All the components were powered through an Eaton 9355 Uninterrupted Power Supply (UPS) system to avoid data loss and abrupt shutdown of the VSM during power failure. Windows interface software was used to control the components and monitor the status of the equipment during measurement. The VSM was calibrated by a standard nickel sphere of known saturation magnetization of 54.7 emu/g [39]. Experimental errors can be reduced by making the calibrating sphere to be of the same size and shape as the samples to be measured [62].

Chapter 4

Magnetic properties of $Mg_{1-x}Zn_xFe_2O_4$ nanoferrites

4.1 Introduction

The magnetic properties of ferrite nanoparticles depend on composition, synthesis techniques and heat treatment. In this chapter we present the results of the variation of the magnetic properties of the $Mg_{1-x}Zn_xFe_2O_4$ nanoferrites where $0 \leq x \leq 1$. We have identified this series of compounds as good candidates for complexing with tetracycline. The presence of zinc would ensure low toxicity of the final complexed nanocomposites. Magnesium is an environmentally friendly element which is also a vital trace element in humans. The aim of the current work is to perform a systematic study of the evolution of the magnetic properties of the $Mg_{1-x}Zn_xFe_2O_4$ system as it is a more environmentally friendly alternative to other ferrites like $Ni_{1-x}Zn_xFe_2O_4$ [24]. It is also interesting to investigate how properties change across the series. We have therefore gradually substituted the magnesium ions by zinc ions starting with the $MgFe_2O_4$ compound. $MgFe_2O_4$ has been reported to exhibit an inverse spinel structure with the Fe^{3+} ions distributed between the tetrahedral (A) and octahedral (B) sites with most of the Mg^{2+} ions occupying the B sites [1]. Zn^{2+} ions have a strong preference for the A site thus when added to the magnesium ferrite will tend to occupy the A sites and the Fe ions will then migrate to the B sites [63]. We expect the cations redistribution to affect the variation of the magnetic,

57

structural and physical properties of the $Mg_{1-x}Zn_xFe_2O_4$ compounds as reported in other systems such as $Cu_{1-x}Zn_xFe_2O_4$ by Akhter et al [3] and in $Mn_{1-x}Zn_xFe_2O_4$ by Dunlap et al [64].

4.2   Results and discussions

4.2.1   X-ray diffraction results

The XRD patterns for the $Mg_{1-x}Zn_xFe_2O_4$ nanoferrites are shown in Figure 4.1. The major peaks correspond to the reflections from the (220), (311), (400), (422), (511) and (440) planes which correspond to the cubic spinel structure with no significant impurity peaks observed. Single phase formation of the compounds is therefore achieved. The measurements were performed on an XRD diffractometer with Cu-K_α radiation of wavelength, $\lambda = 1.5406$ nm. The crystallite sizes of the nanoferrites were estimated from the peak broadening of the most intense (311) peak using the Scherrer equation (3.4.4). The lattice parameters of the nanoferrites were also calculated from the XRD data using equation (3.4.3). The XRD densities for various x values were calculated from the lattice parameters and molecular weights of the individual nanoferrites using equation (3.4.5). In Table 4.1, we present the results of the crystallite sizes D, lattice parameters a and XRD densities ρ_{XRD}.

Figure 4.2 shows the variation of crystallite sizes and lattice parameters as a function of the Zn-concentration, x. The crystallite sizes lie between 10.5 and 22.5 nm with the largest crystallite for the composition with $x = 0.6$. The method of washing by sedimenting the precipitate used in the current series of compounds (section 3.2) appears to affect the range of crystallite sizes. For another $Mg_{0.5}Zn_{0.5}Fe_2O_4$ sample that was washed and filtered using glass microfibre GF/F Whatman filters, a much lower crystallite size of 8.0 nm was obtained. An increase in the lattice parameter with increasing x is also observed which we attribute to the replacement of the smaller Mg^{2+} (0.66 Å) ions by the larger Zn^{2+} (0.86 Å) ions [1, 65, 66]. There is an overall expansion of the unit cell due to the introduction of an ion with larger radius. Similar results have also been observed in the Zn-Mg [67], Li-Mg [68] and Li-Cd [69] ferrites.

58
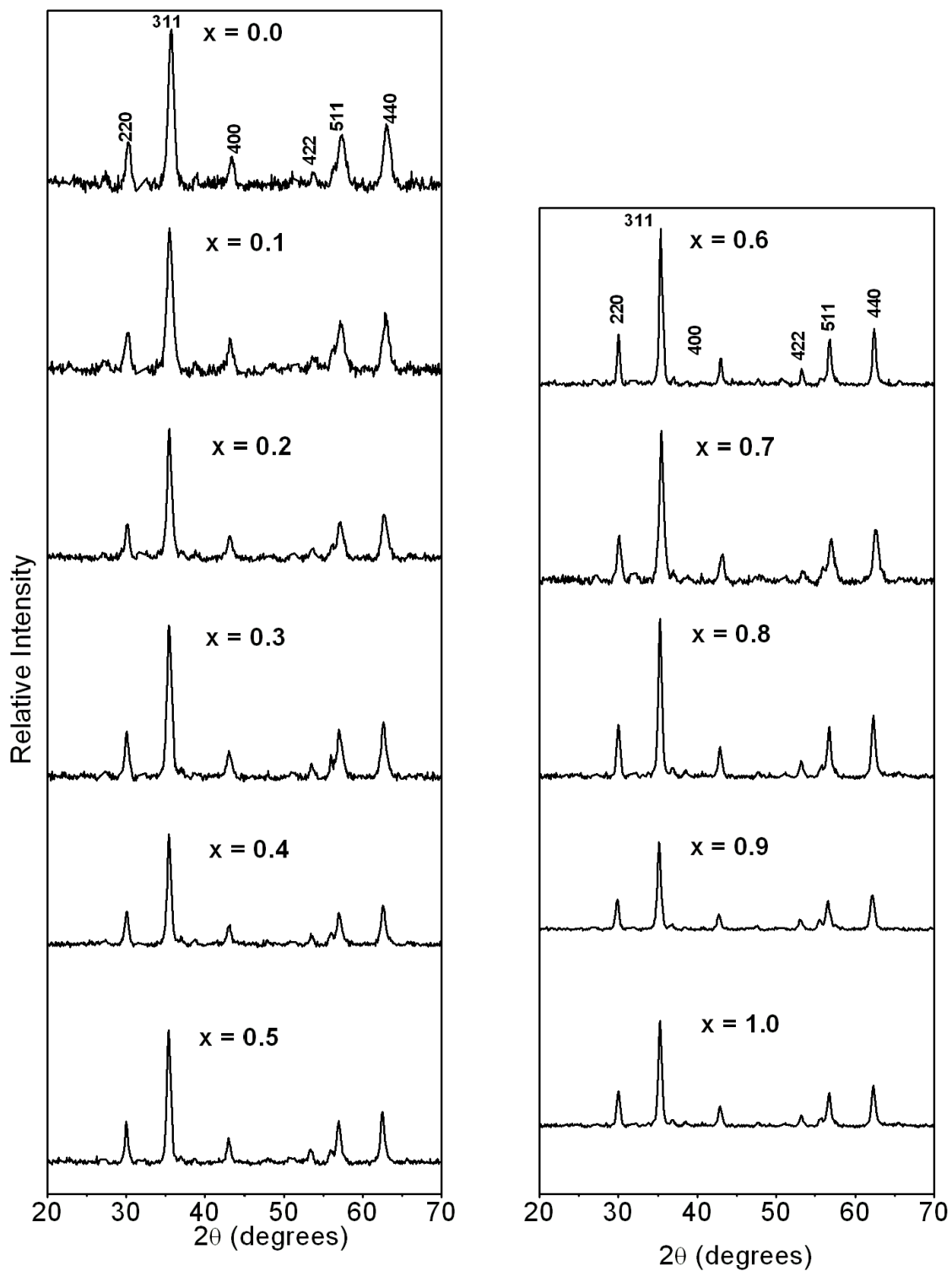
Figure 4.1: XRD patterns of the $Mg_{1-x}Zn_xFe_2O_4$ nanoferrites.

Table 4.1: Crystallite sizes D, lattice parameters a and XRD densities ρ_{XRD} for $Mg_{1-x}Zn_xFe_2O_4$ nanoparticles.

x	D (nm) ± 0.02	a (Å) $\pm 10^{-3}$	ρ_{XRD} (g/cm^3) ± 0.02
0.0	11.49	8.339	4.58
0.1	10.60	8.375	4.62
0.2	14.38	8.384	4.70
0.3	13.70	8.380	4.80
0.4	16.35	8.393	4.86
0.5	16.28	8.396	4.95
0.6	22.24	8.419	5.00
0.7	14.51	8.393	5.14
0.8	18.48	8.431	5.16
0.9	18.00	8.461	5.20
1.0	18.34	8.421	5.34
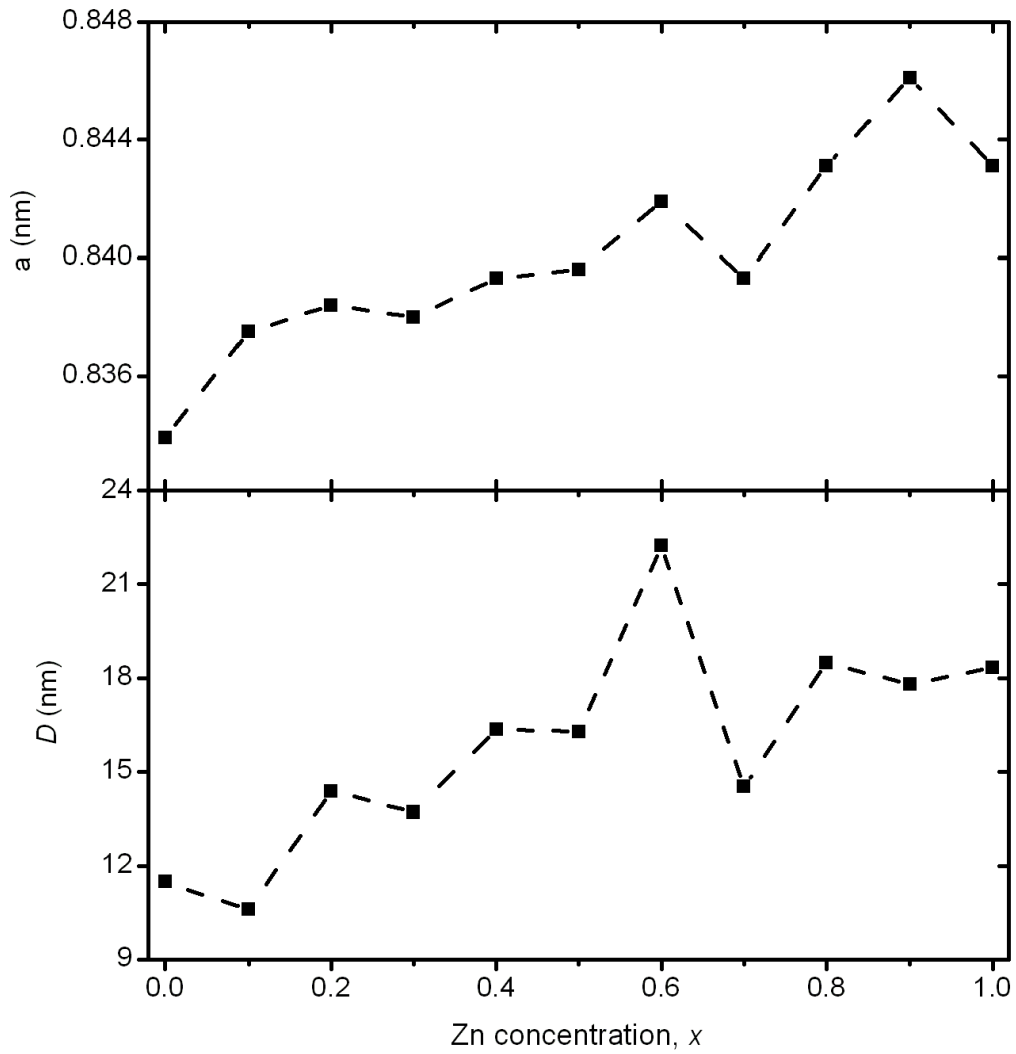
Figure 4.2: Crystallite sizes D and lattice parameters a for $Mg_{1-x}Zn_xFe_2O_4$ nano-ferrites.

Figure 4.3 shows the variation of the XRD density (ρ_{XRD}) as a function of Zn content, x. We have investigated this because it is well known that density plays an important role in controlling the properties of ferrites [70]. ρ_{XRD} depends on the molecular weight and lattice parameter of the sample. Figure 4.3 suggests that the XRD density is strongly dependent on the Zn-concentration. We observe a linear increase in ρ_{XRD} with x with a correlation coefficient of 0.9955.

4.2.2 Mössbauer spectroscopy results

Room temperature Mössbauer spectra for the $Mg_{1-x}Zn_xFe_2O_4$ nanoferrites are given in Figure 4.4. The data points correspond to the experimental data and the solids lines represent fits to the data. The fits are based on the Lorentzian site analysis by using Recoil Mössbauer analysis software. All the spectra were calibrated with respect to alpha-iron spectrum at room temperature. The spectra were fitted by at least two sextets and one doublet which represent the fraction of the Fe ions at both the tetrahedral and octahedral sites. The sextets represents the Fe^{3+} ions in a ferrimagnetic state whilst the doublets represents the Fe^{3+} ions in paramagnetic state [2]. The spectra indicate that the samples for $x \leq 0.7$ were magnetically ordered and thus were fitted by the two sextets. The sextet with the higher magnetic field was assigned to the octahedral site due to the dipolar fields resulting from the deviation from cubic symmetry and from the covalent nature of the tetrahedral bonds [1, 71]. Paramagnetic behavior was observed for $x > 0.7$ and thus the spectra were fitted by two doublets. Each doublet represents the paramagnetic state for the Fe at tetrahedral or octahedral site. The doublets were assigned to A or B sites by the values of their isomer shifts. The smaller isomer shift was assigned to the tetrahedral site. Various parameters obtained during the Mössbauer spectra analysis including isomer shifts, line widths, hyperfine fields and site populations for the fitted sextets and doublets are presented in Table 4.2. The range of the values of the isomer shifts is consistent with Fe^{3+} ions [72]. Figure 4.5 shows the variation of isomer shifts at A and B sites respectively. This confirms the lower isomer shift on the A site than at B site due to the higher covalency of the Fe-O bond on the A site [2]. The magnetic hyperfine fields for $x \leq 0.7$ are shown in Figure 4.6. A decrease in the hyperfine
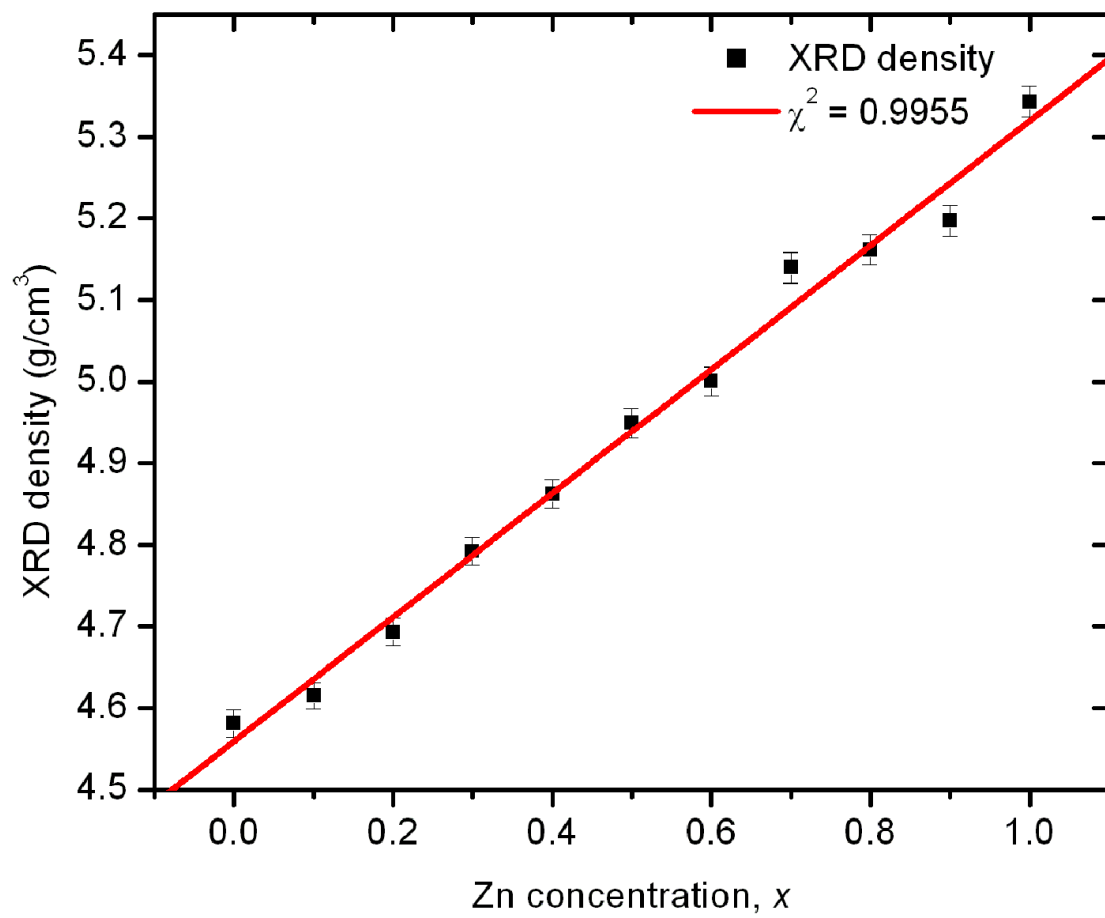
Figure 4.3: XRD density ρ_{XRD} for $Mg_{1-x}Zn_xFe_2O_4$ nanoferrites.
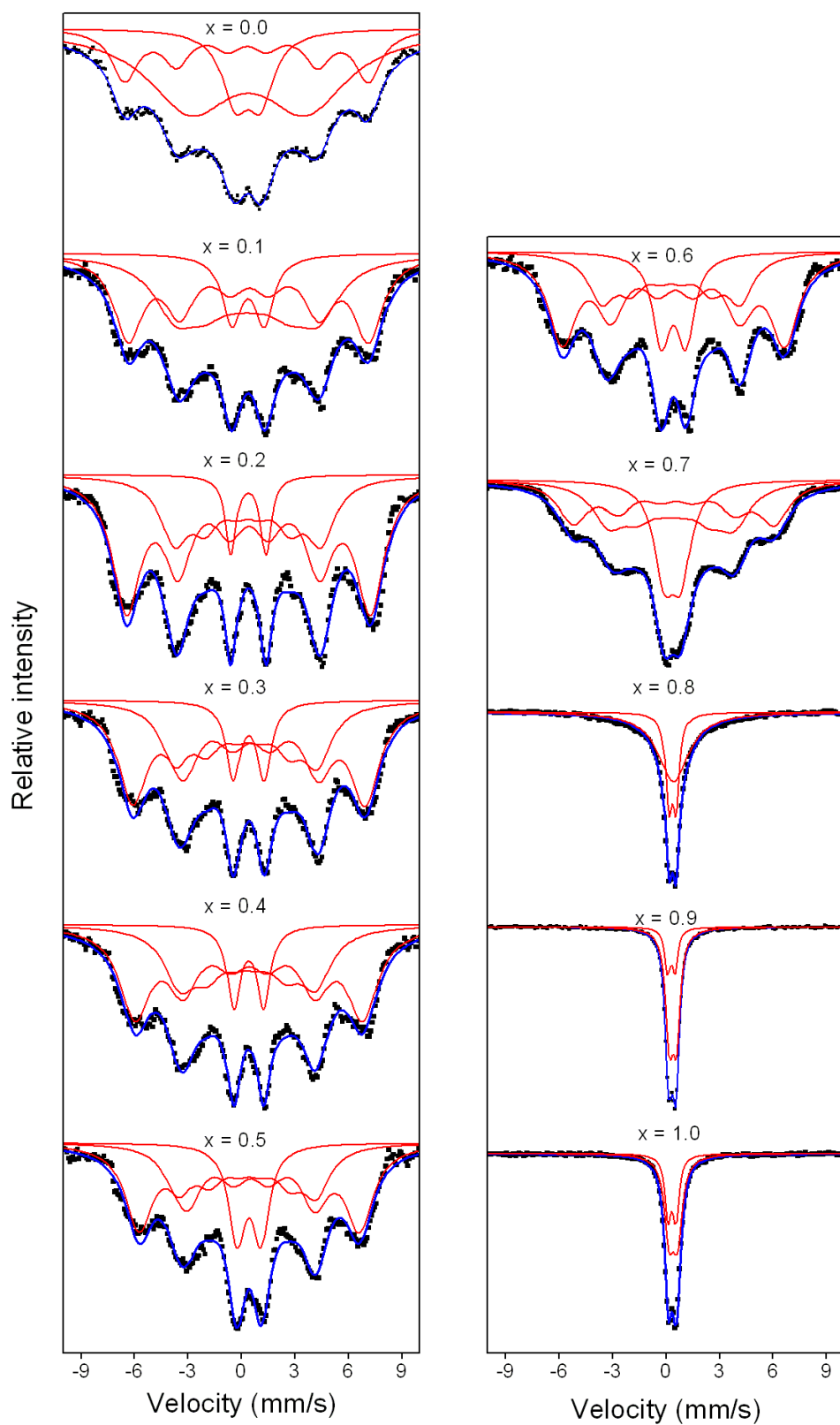
Figure 4.4: Mössbauer spectra for $Mg_{1-x}Zn_xFe_2O_4$ nanoferrites.

64

Table 4.2: Isomer shifts δ, line widths Γ, hyperfine fields B and Fe^{3+} site populations f for $Mg_{1-x}Zn_xFe_2O_4$ nanoparticles.

x	δ (mm/s)			Γ (mm/s)		B (T)		f (%)		
	δ_A	δ_B	δ_D	Γ_A	Γ_B	B_A	B_B	f_A	f_B	f_D
	± 0.06	± 0.04	± 0.02	± 0.08	± 0.06	± 0.4	± 0.2			
0.0	0.29	0.40	0.32	1.69	1.04	24.4	42.0	46.3	37.0	16.7
0.1	0.30	0.41	0.36	1.46	0.97	24.9	41.8	42.3	45.4	12.3
0.2	0.34	0.39	0.38	0.94	0.94	25.4	42.4	29.4	63.3	7.3
0.3	0.31	0.47	0.40	0.96	0.98	24.7	40.4	32.2	56.9	10.9
0.4	0.32	0.41	0.40	1.05	1.02	23.7	39.5	33.9	55.0	11.1
0.5	0.38	0.48	0.41	0.92	0.93	24.1	38.3	29.3	52.7	18.0
0.6	0.27	0.46	0.42	0.89	0.94	24.1	38.6	27.0	55.6	17.4
0.7	0.37	0.50	0.36	1.09	1.01	21.7	35.0	37.4	36.5	26.1
0.8	0.35	0.41	-	0.22	1.03	-	-	33.9	66.1	-
0.9	0.30	0.39	-	0.19	0.25	-	-	23.1	76.9	-
1.0	0.33	0.40	-	0.21	0.32	-	-	34.3	65.7	-
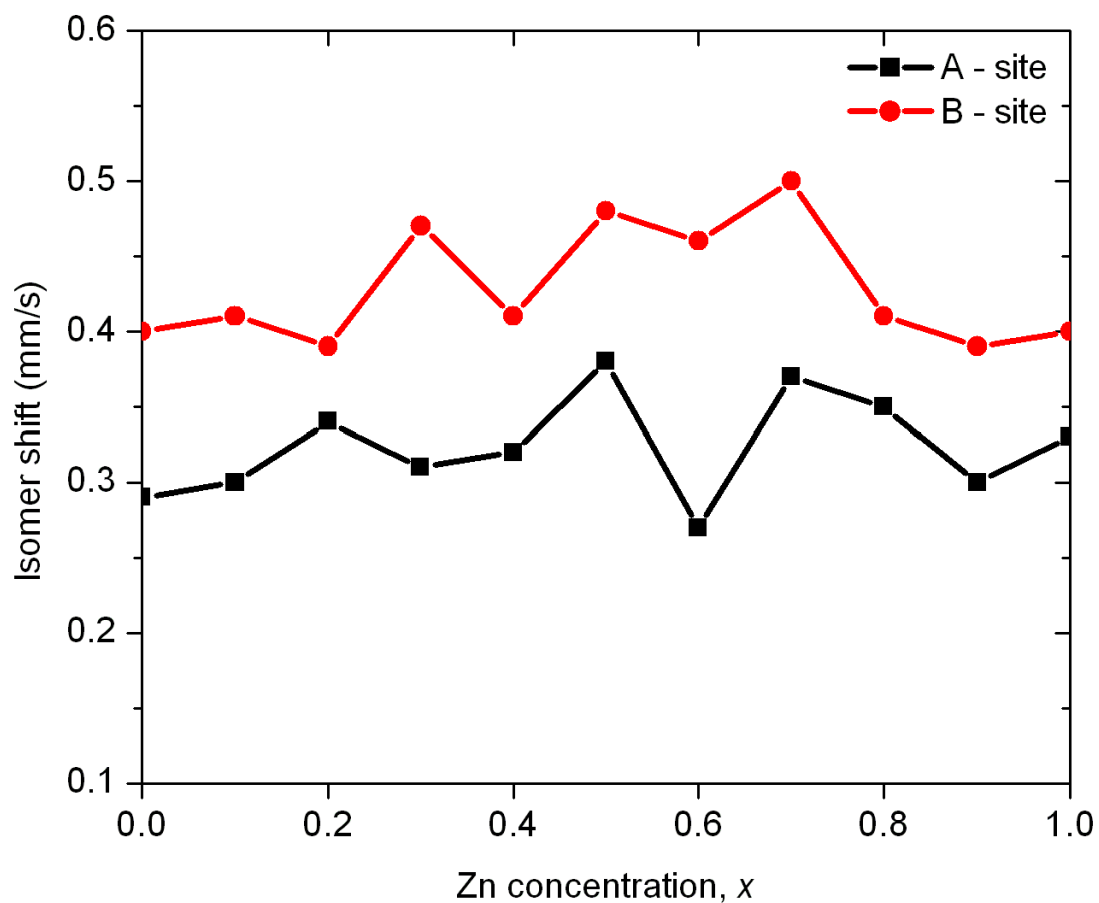
Figure 4.5: Isomer shifts associated with the Fe^{3+} ions at A and B sites for the $Mg_{1-x}Zn_xFe_2O_4$ nanoferrites.
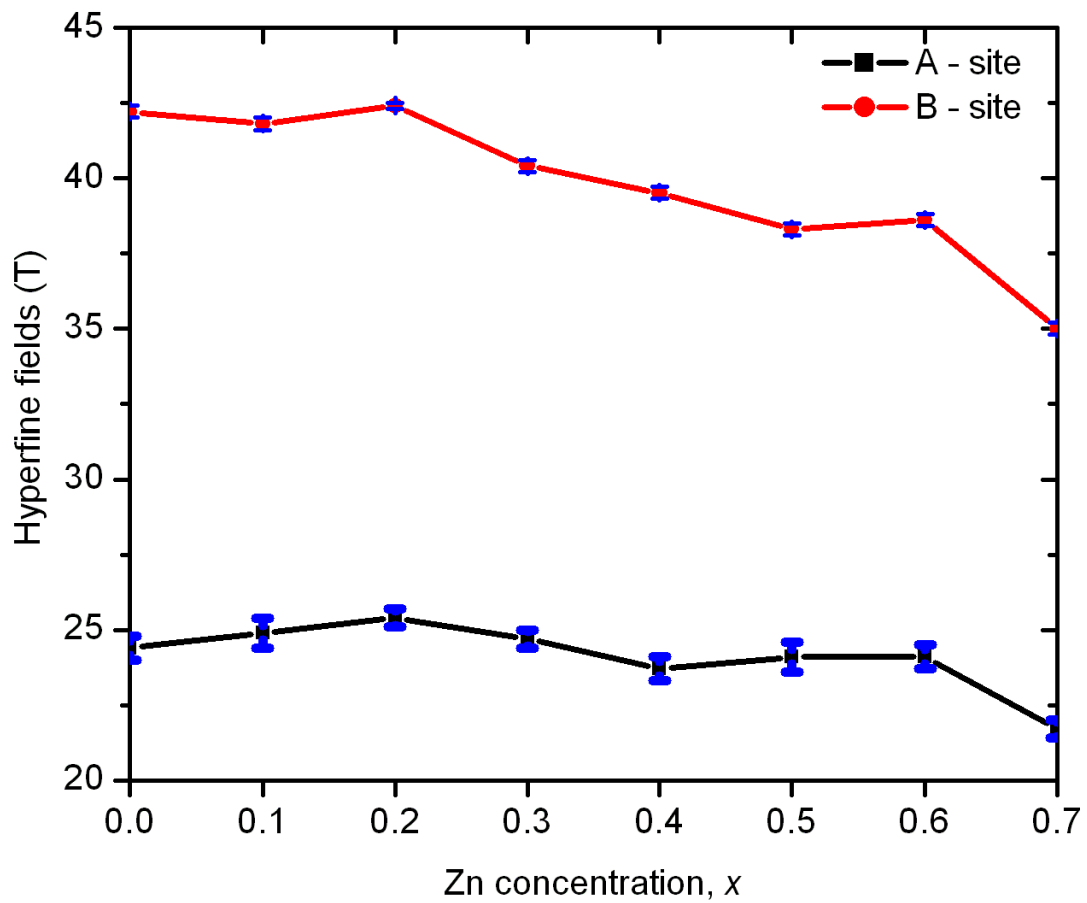
Figure 4.6: Hyperfine fields at A and B sites associated with Fe^{3+} ions in $Mg_{1-x}Zn_xFe_2O_4$ nanoferrites.

fields with higher Zn content was observed at both sites in agreement with the results by Gismelseed et al [1]. The decrease of the hyperfine fields is due to the dilution of the system by non-magnetic Zn ions [73].

4.2.3 Magnetization results

Figure 4.7 shows the room temperature hysteresis loops of the $Mg_{1-x}Zn_xFe_2O_4$ nano-ferrites which are consistent with superparamagnetic behaviour. The maximum applied external field during the measurements was 14 kOe. We can identify two groups of compounds ($x = 0.8$, 0.9 and 1.0) with maximum isothermal magnetizations below 40 emu/g and another group ($x \leq 0.7$) with magnetizations above 60 emu/g at 14 kOe. The former group ($x > 0.7$) was associated with paramagnetic phases from Mössbauer spectroscopy measurements. The S-shape magnetizations in the paramagnetic state suggests the presence of superparamagnetic clusters even above the Curie points. Figure 4.8 shows the initial magnetization curves of the nanoferrites which were fitted by equation (2.5.2). The magnetic moment per molecule (μ) in units of μ_B was calculated from the equation

$$\mu = \frac{M_o M_s}{5585} \qquad (4.2.1)$$

where M_o is the molecular mass of the sample in grams [74, 75]. The squareness ratio (SQR) which provides a good distinction between soft and hard magnetic materials was also calculated from the equation

$$SQR = \frac{M_r}{M_s}. \qquad (4.2.2)$$

Several magnetic properties parameters were determined from the magnetization data. These are presented in Table 4.3 and the magnetizations plotted in Figure 4.9. An increasing trend in the saturation magnetization was observed with increasing x for $x \leq 0.5$. For $x > 0.5$, there is a decreasing trend for magnetizations. The lowest saturation magnetization is 6.1 ± 0.1 emu/g for $x = 0.9$. All the compositions for $x \leq 0.7$ have higher saturation magnetization (above 50 emu/g) with the highest of 71.4 ± 0.1 emu/g for $x = 0.5$. Low values of the SQR and coercivity were obtained

68
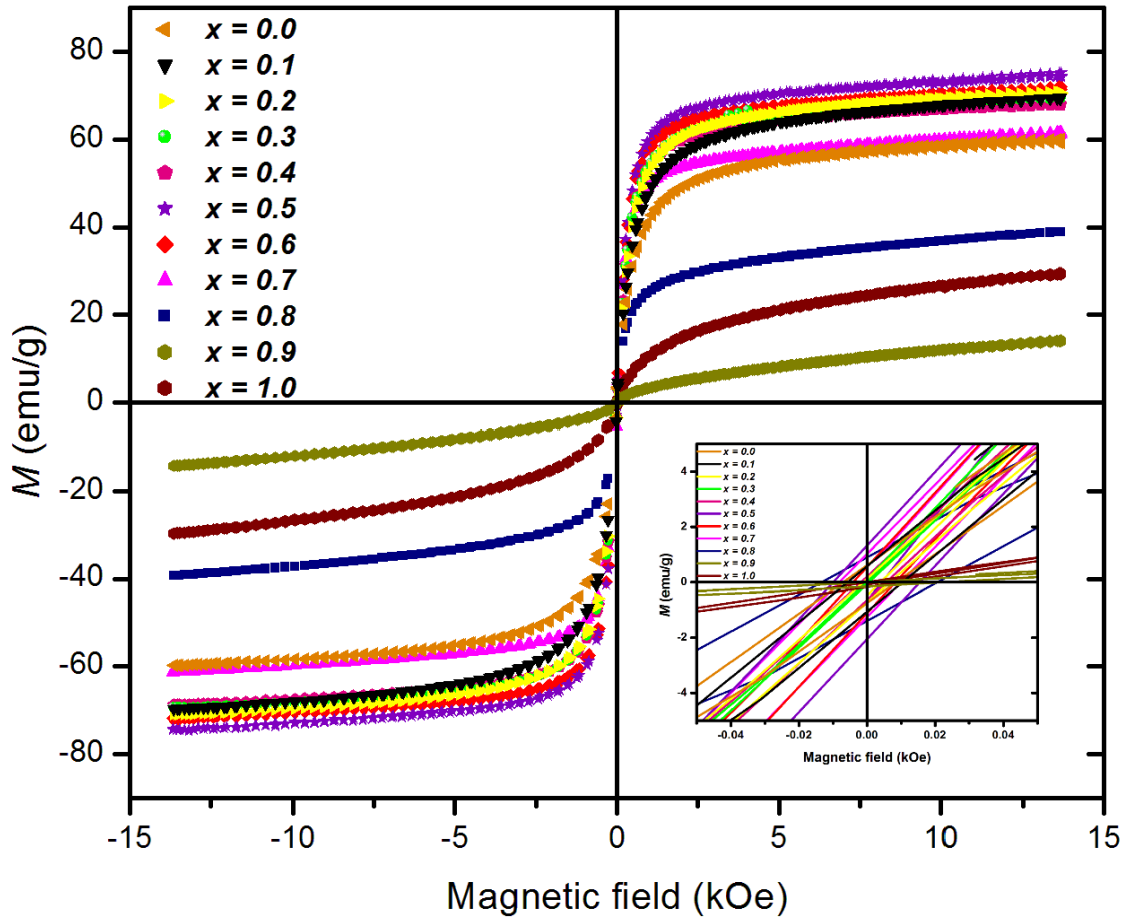
Figure 4.7: Hysteresis loops of the $Mg_{1-x}Zn_xFe_2O_4$ nanoferrites. The insert shows hysteresis in the field range -0.05 kOe $\leq H \leq$ 0.05 kOe.
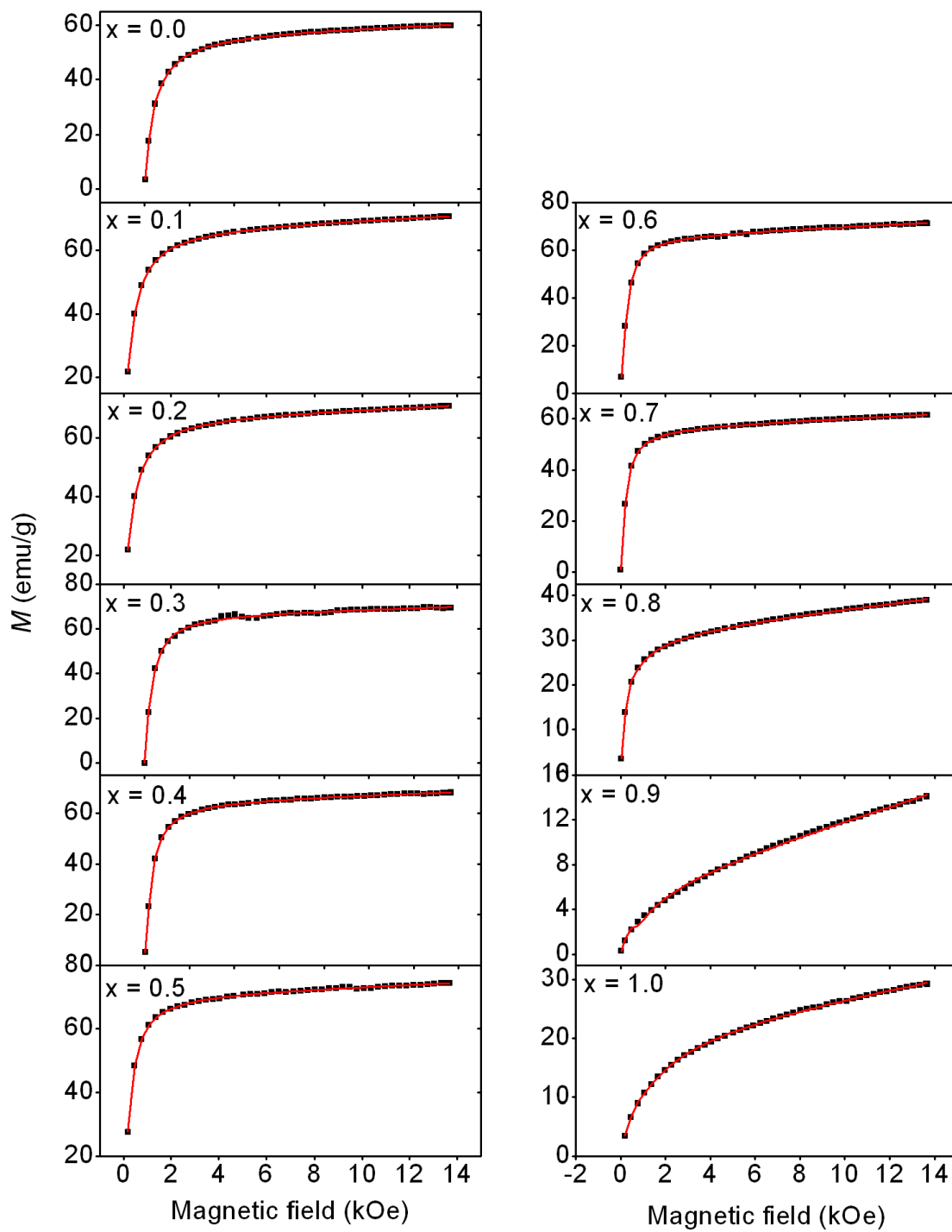
Figure 4.8: The initial magnetization curves for the $Mg_{1-x}Zn_xFe_2O_4$ nanoferrites fitted by equation (2.5.2).

Table 4.3: Saturation magnetization M_s, maximum magnetization M_m, remanent magnetization M_r, coercive fields H_C and magnetic moment per molecule μ for the $\text{Mg}_{1-x}\text{Zn}_x\text{Fe}_2\text{O}_4$ nanoferrites.

x	M_s (emu/g) ± 0.1	M_m (emu/g) ± 0.1	M_r (emu/g) ± 0.05	H_C (Oe) ± 0.5	μ (μ_B) ± 0.04	M_r/M_s
0.0	58.2	59.8	0.68	8.6	2.08	0.0117
0.1	67.1	69.6	0.82	8.0	2.45	0.0122
0.2	68.0	70.8	0.43	4.6	2.54	0.0063
0.3	67.6	69.5	0.05	4.7	2.57	0.0007
0.4	65.7	68.4	0.42	8.3	2.55	0.0064
0.5	71.4	74.8	1.68	12.8	2.82	0.0235
0.6	66.5	71.9	0.83	6.5	2.67	0.0124
0.7	56.6	61.4	1.14	8.9	2.32	0.0201
0.8	32.0	39.1	1.14	17.8	1.33	0.0356
0.9	6.1	14.2	0.08	11.8	0.26	0.0131
1.0	22.0	29.6	0.09	4.3	0.95	0.0040
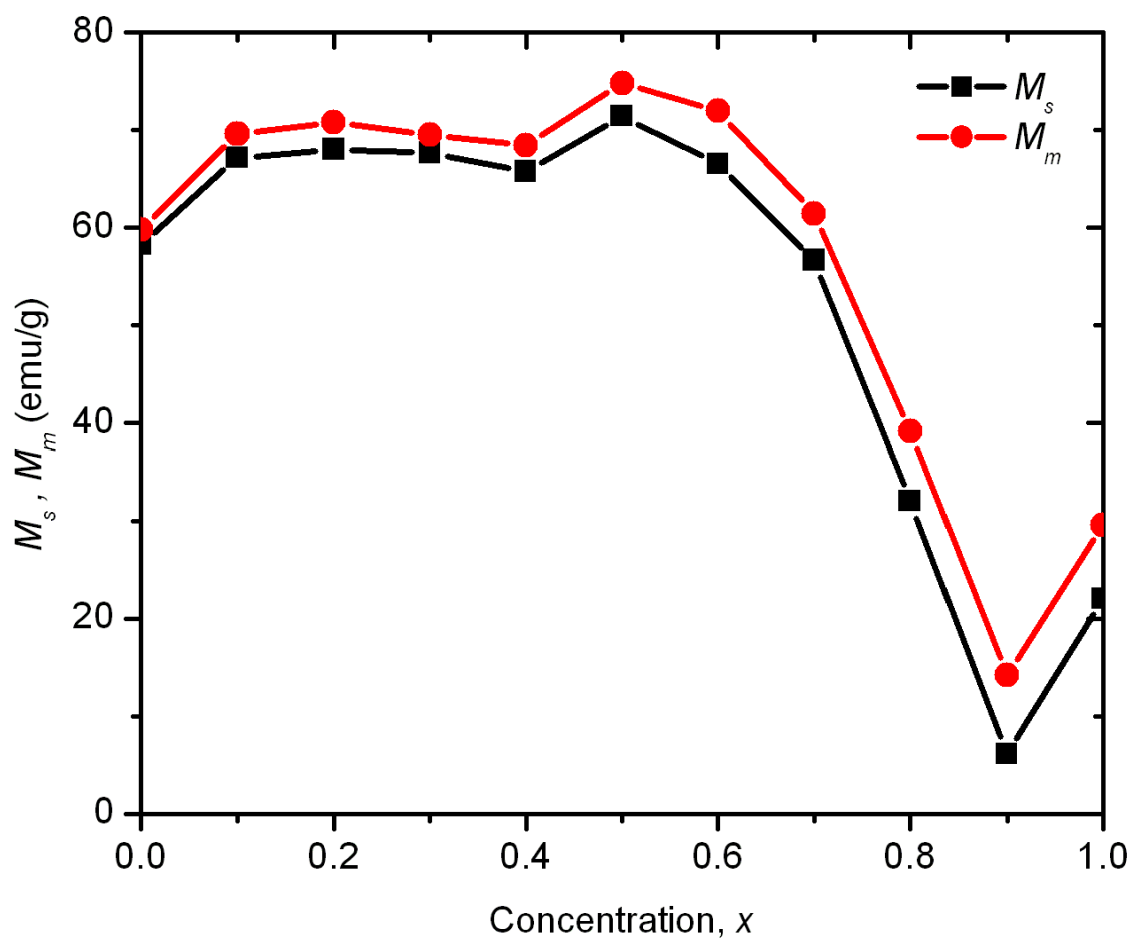
Figure 4.9: Saturation magnetization M_s and maximum magnetization M_m for the Mg$_{1-x}$Zn$_x$Fe$_2$O$_4$ nanoferrites.

for all the compositions which indicate soft magnetic properties of the compounds. The coercive field is a very important parameter as it is a measure of magnetization reversal process under the action of an applied field. The low values also suggest the existence of small magnetic particles in the form of single domains [76].

4.3   Conclusions

We have successfully made $Mg_{1-x}Zn_xFe_2O_4$ nanoferrites using glycol-thermal method. XRD results show single phase cubic spinel structure for all the compositions with no impurity peaks. Crystallite sizes were obtained in the range 10.5 - 22.5 nm which appear to be influenced by the method of washing the precipitates. A gradual increase in the lattice parameter was observed with increasing Zn content x as evidence that the smaller Mg^{2+} ions were being replaced by the bigger Zn^{2+} ions leading to the expansion of the unit cell. We have also found a strong correlation between the XRD density with Zn concentration x. The Mössbauer spectra recorded at room temperature show transformation from ordered ferrimagnetic state to paramagnetic state with increase in Zn content. Analysis of the spectra show Fe^{3+} ions at both tetrahedral (A) and octahedral (B) sites. The isothermal magnetizations at room temperature show evidence of superparamagnetic behaviour of the compounds. It is interesting to note that starting with $ZnFe_2O_4$, slightly doping with Mg causes a drastic reduction in the saturation magnetization. Magnetization results show a peak in the saturation magnetizations at $x = 0.5$ which is the composition with equal concentration of zinc and magnesium. The compound $Mg_{0.5}Zn_{0.5}Fe_2O_4$ has therefore been selected as the best choice for complexing with tetracycline.

Chapter 5

Magnetic properties of Tetracycline-Mg$_{0.5}$Zn$_{0.5}$Fe$_2$O$_4$ composites

5.1 Introduction

One of the objectives of studying the magnetic properties of the Mg$_{1-x}$Zn$_x$Fe$_2$O$_4$ system was to choose a composition with suitable magnetic properties to complex with tetracycline. The intention was to improve the bioactivity of the antibiotic properties of tetracycline against a range of bacteria. We have selected the composition corresponding to $x = 0.5$ for this purpose.

Tetracyclines are a group of antibiotics used in the treatment of infections in the urinary track and intestines [77]. They have been used in humans and veterinary medicine for many decades and still provide effective treatment for some specific conditions like moderately severe acne and rosacea. However, bacterial resistance has reduced the effectiveness of tetracyclines in many instances. Tetracyclines have a planar structure consisting of four hydrophilic groups on one face and hydrophobic groups on the other face. In our study we have used tetracycline-HCl which is used to treat many gram-negative and gram-positive bacteria and some protozoa [78]. In this chapter we present the structural and magnetic properties of tetracycline-Mg$_{0.5}$Zn$_{0.5}$Fe$_2$O$_4$ nanoferrites (Tet-NF) produced by high-energy ball milling under

argon and air environments. The starting materials initially had different crystal structures. It is interesting to investigate the evolution of the structure of the Tet-NF composites as a function of the milling time. Another important aspect of the study is to investigate the site preference of tetracycline in the cubic spinel structure. The experimental details for the formation of the Tet-NF nano-composites are discussed in section 3.3.

5.2 Results and discussions

5.2.1 X-ray diffraction results

Figure 5.1 shows the XRD spectra for the milled Tet-NF with reference to the original unmilled $Mg_{0.5}Zn_{0.5}Fe_2O_4$ and tetracycline hydrochloride. The XRD results show that the Tet-NF complexes into the cubic spinel structure without significant changes in the peak positions, intensity and line width compared to the $Mg_{0.5}Zn_{0.5}Fe_2O_4$ nanoferrite. However, the milling environment seems to have an effect on the results. An impurity peak develops around $2\theta = 58°$ with increased milling time to 5 h. This is more prominent in samples milled in air atmosphere. The impurity peak disappears in both air and argon environments after milling for at least 15 h. We attribute this to a transient impurity probably due to the oxidation of the drug. We therefore do not find evidence for contamination of the Tet-NF from the grinding surfaces of the hardened steel jars and balls used. No significant changes in the masses of the grinding balls were observed before and after milling for 30 h.

The crystallite sizes were deduced from the most intense (311) XRD peak using the Scherrer equation. The lattice parameters were determined from the XRD patterns using Bragg's law. Table 5.1 shows the calculated crystallite sizes D and the lattice parameters a for the Tet-NF composites as a function of milling time (MT) for both air and argon atmospheres. The associated changes are illustrated in Figure 5.2. The results show that the milling atmosphere has an effect in controlling the variation of the crystallite sizes and lattice parameters. Smaller variations are observed for the argon milled composites compared to the samples milled in air.
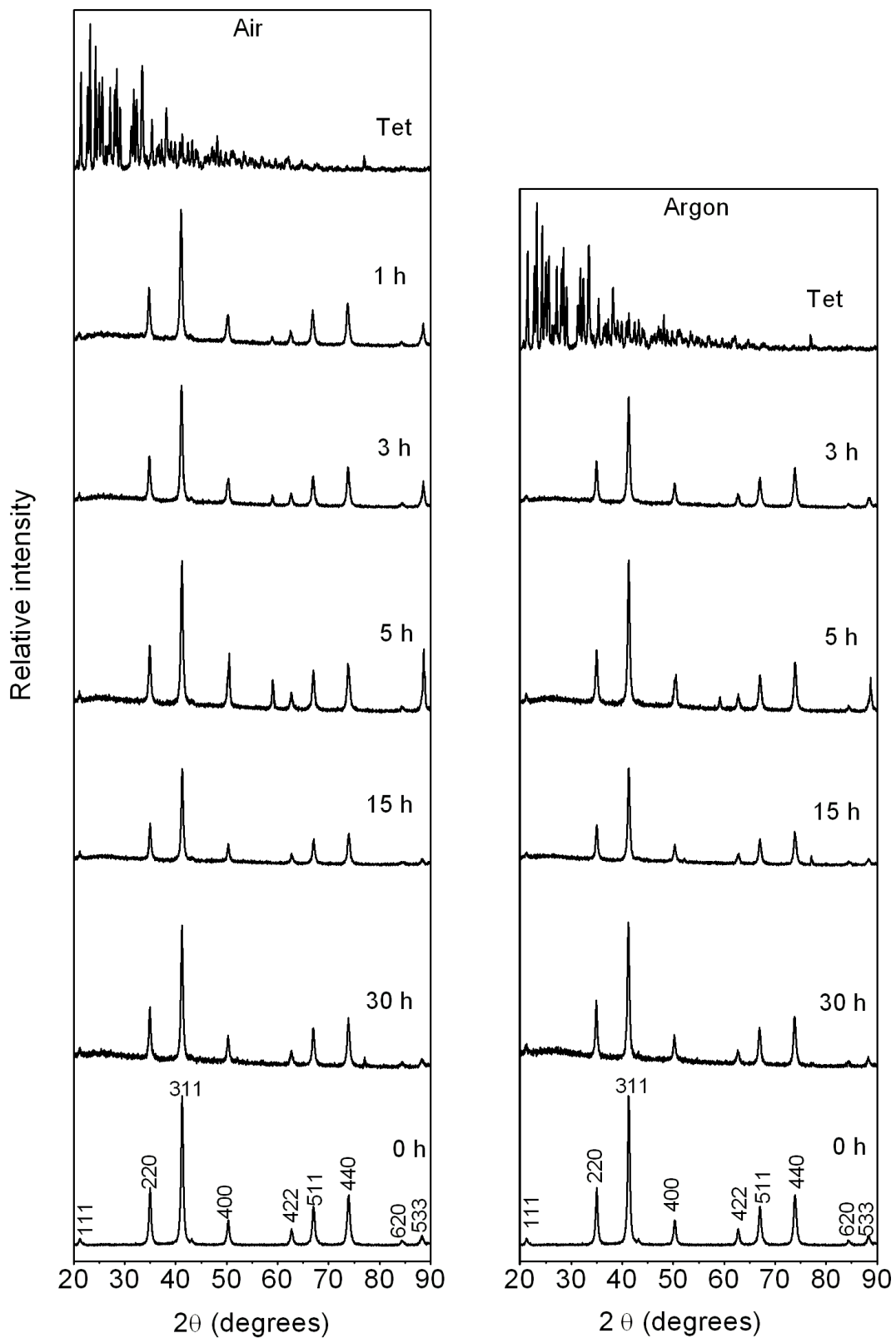
Figure 5.1: XRD patterns of un-milled tetracycline-HCl (Tet), un-milled nanoferrite (0 h), and milled Tet-NF composites in air and argon atmospheres.

Table 5.1: Variation of crystallite sizes D and lattice parameters a for the Tet-NF composites milled under air and argon atmospheres for different milling time (MT).

MT	Air		Argon	
(h)	D (nm)	a (Å)	D (nm)	a (Å)
	±0.04	±0.0002	±0.02	±0.0002
0	20.35	8.4260	20.35	8.4260
1	21.17	8.4640	-	-
3	20.89	8.4495	20.18	8.4357
5	20.77	8.4362	21.65	8.4316
15	22.39	8.4235	21.70	8.4289
30	38.52	8.4338	21.44	8.4405
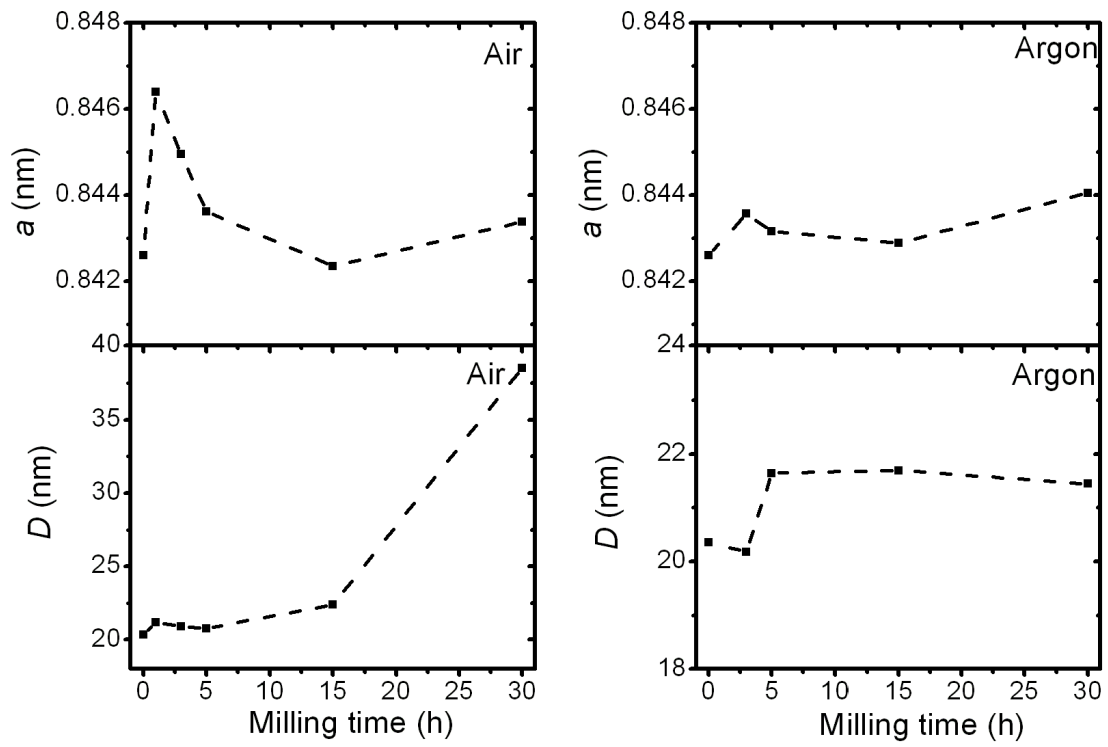
Figure 5.2: Crystallite sizes D and the lattice parameters a for the unmilled nano-ferrite and for milled Tet-NF composites.

5.2.2 Mössbauer spectroscopy results

Room temperature Mössbauer spectroscopy measurements were performed in zero applied magnetic field. The Mössbauer spectra provide more information about the magnetic state of the nanocomposites and the Fe^{3+} ion distribution amongst the interstitial sites. This will give us information on how tetracycline is complexed into the spinel structure of the $Mg_{0.5}Zn_{0.5}Fe_2O_4$ nanoferrite. Figure 5.3 shows the ^{57}Fe Mössbauer spectra of the samples obtained for different milling times and atmospheres. As before the velocity calibrations for the Mössbauer spectra were performed with respect to the α-Fe spectra at room temperature and the analysis by Recoil Mössbauer analysis software. All the quoted isomer shifts in this study are therefore with respect to that of α-Fe. The Voight-based fitting (VBF) analysis was used to extract the magnetic parameters of the samples since it provides reliable information on cation distribution. Zn^{2+} ions are known to have strong preference for the A sites [5, 79]. Although Mg^{2+} ions prefer the B sites, about 10% of the ions have been reported to be located at the A-sites as well for $MgFe_2O_4$ and $Mg_{0.5}Zn_{0.5}Fe_2O_4$ ferrites [1, 80, 81]. We have therefore assumed the cation distribution of the form: $\left(Zn_{0.5}^{2+}Fe_y^{3+}Mg_x^{2+}\right)_A \left[Mg_{0.5-x}^{2+}Fe_{2-y}^{3+}\right]_B$ for our $Mg_{0.5}Zn_{0.5}Fe_2O_4$ nanoferrite where $x \approx 0.1$ and y are the proportions of Mg^{2+} and Fe^{3+} ions in the interstitial sites [81].

Each spectrum was fitted by two sextets and a central doublet which we assume arises from the superparamagnetic (SPM) behaviour of the Fe^{3+} ions in the ultra-dispersed ferrite particles [82]. The two sextets represent the magnetically ordered Fe^{3+} ions in the tetrahedral (A) and octahedral (B) sites. The spectra for the milled Tet-NF composites are similar for both air and argon atmospheres thus the milling time seems to only have a slight effect. Figure 5.4 show more revealing plots of the superposition of the hyperfine field distributions associated with the tetrahedral (A) and octahedral (B) sites for the unmilled nanoferrite and milled Tet-NF composites in air and argon atmospheres.

Lower hyperfine field shifts are observed between the unmilled nanoferrite and the 1 h air milled Tet-NF composite. Further milling (3, 5, 15 and 30 h) in air atmosphere does not yield any hyperfine fields shifts but the plots appear superim-
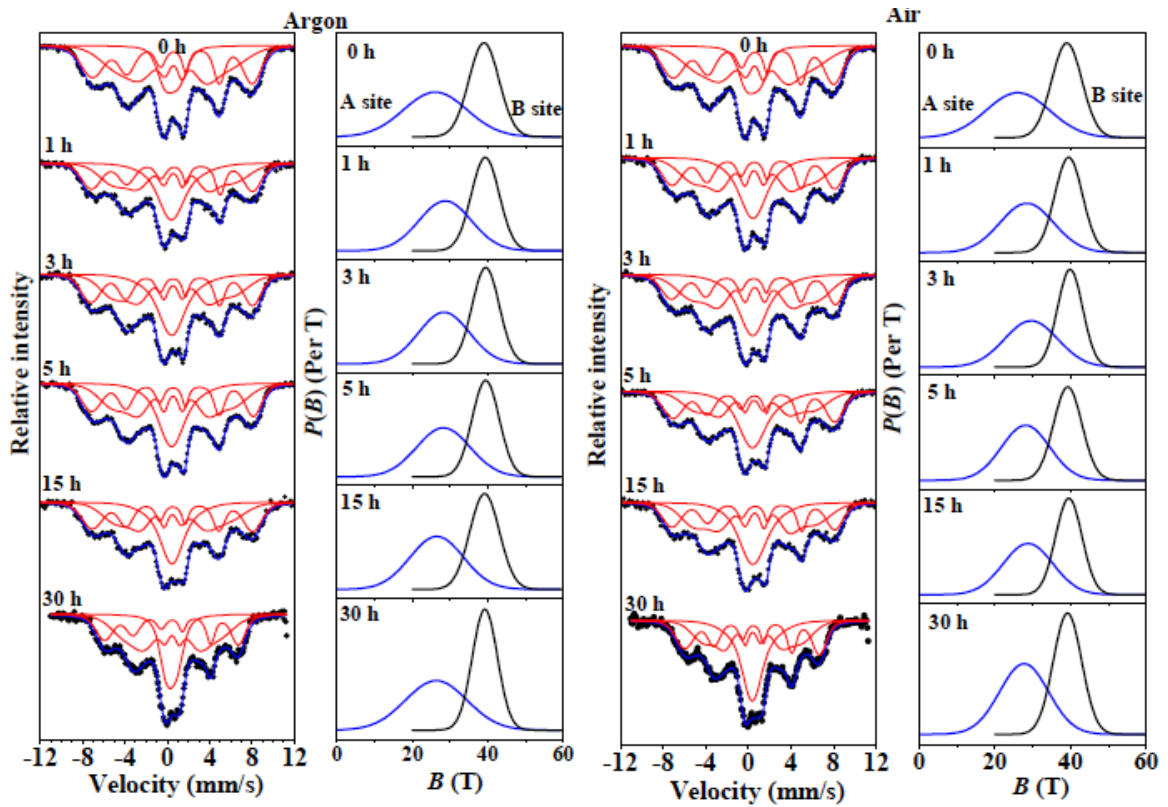
Figure 5.3: Room temperature Mössbauer spectra and their corresponding hyperfine field distributions for the unmilled nanoferrite and milled Tet-NF composites in air and argon atmospheres.
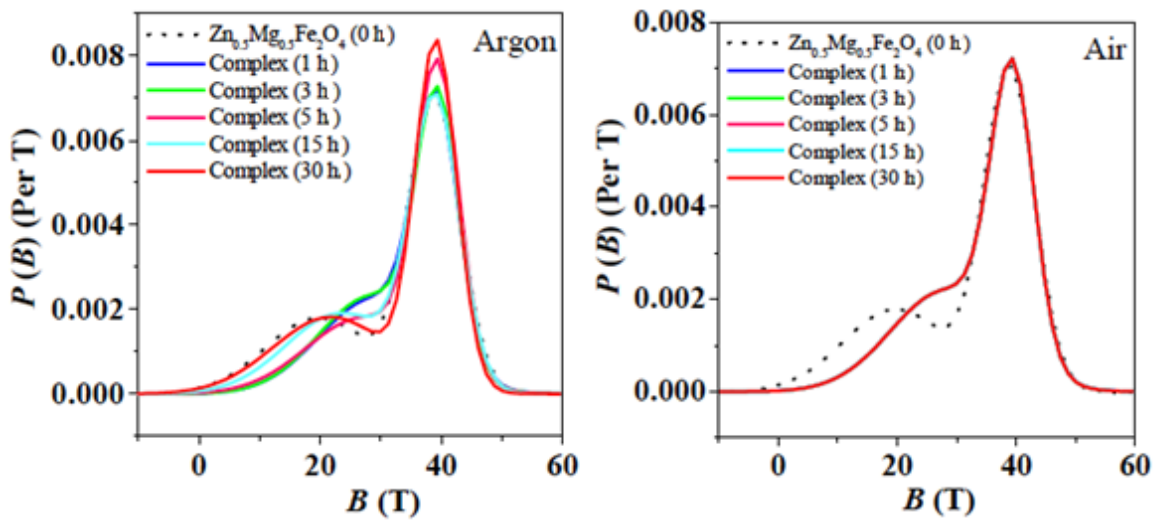
Figure 5.4: Superposition of hyperfine field distributions for the unmilled nanoferrite and milled Tet-NF composites in air and argon atmospheres.

posed upon each other and clearly only the tetrahedral (A) site Fe^{3+} ions seem to be influenced by the milling. Similar trends in lower hyperfine field shifts between the unmilled nanoferrite and the argon milled Tet-NF (1, 3 and 5 h) composite are observed. Further milling in argon atmosphere (15 h and 30 h) yields shifts in both lower and higher hyperfine fields. The changes in hyperfine fields in both the tetrahedral (A) and octahedral (B) sites for the argon milled composites suggests less covalent bonding between the ions as compared to the air milled composites.

Tables 5.2 and 5.3 present the magnetic parameters extracted from the spectral analysis using the VBF site analysis model. The sextet with higher hyperfine fields was assigned to the octahedral (B) site due to the dipolar fields resulting from the deviation from the cubic symmetry [1, 71]. The sextet with lower hyperfine field was assigned to the tetrahedral (A) site. Figure 5.5 shows the variation of the hyperfine fields on the tetrahedral (A) and octahedral (B) sites for the unmilled ferrite (0 h) and the milled Tet-NF composites in air and argon atmospheres respectively.

There is an increase in the average hyperfine fields on both A and B sites after 1 h of milling compared to the unmilled nanoferrite. The increase is more on A site and with further milling the average field reduces on A site. On the B site the increase is slightly less and remain almost constant on further milling. We therefore suspect that the tetracycline is complexing more with ions on the tetrahedral (A) site than on the octahedral (B) site.

The values of the isomer shifts are in the range 0.37 - 0.50 mm/s. This is consistent with Fe^{3+} ions on both A and B sites [72]. Our results also show slightly higher isomer shift values on the A site than on B site which was not expected as in many cases we usually have the trend $\delta_A < \delta_B$. Similar results where $\delta_A > \delta_B$ have been reported by Gismelseed et al [1] in the $Zn_xMg_{1-x}Fe_2O_4$ system for $x = 0.4$ and 0.5. A significant increase in the doublet areas is evident for both milling atmospheres; from 16% to 26% for air atmosphere and from 16% to 28% for argon atmosphere after only 1 h of milling. This is about 10% and 12% increase in the doublet areas for air and argon atmospheres respectively. The doublet area increases further due to milling in air atmosphere to reach a maximum of 32% whilst further milling in argon atmosphere decreases the doublet area to 24%. This strongly suggest

Table 5.2: Average isomer shifts δ, hyperfine fields B and quadrupole splitting Δ for the unmilled nanoferrite (0 h) and the milled Tet-NF composites (1, 3, 5, 15 and 30 h) in air and argon atmospheres. Tetrahedral (A), Octahedral (B) and superparamagnetic (Db) sites.

MT	$<\delta>$			$<B>$		$<\Delta>$
(h)	(mm/s)			(T)		(mm/s)
Argon	δ_A	δ_B	δ_{Db}	B_A	B_B	Δ_{Dd}
	±0.04	±0.02	±0.05	±2.7	±0.6	±0.05
0	0.46	0.43	0.37	26.1	39.0	1.10
1	0.47	0.43	0.46	28.7	39.3	-0.29
3	0.46	0.39	0.37	28.4	39.5	-0.04
5	0.46	0.42	0.46	28.2	39.5	0.25
15	0.40	0.42	0.37	26.5	39.2	0.03
30	0.47	0.42	0.39	26.3	39.2	-0.98
Air	δ_A	δ_B	δ_{Db}	B_A	B_B	Δ_{Dd}
	±0.04	±0.02	±0.05	±2.7	±0.6	±0.05
0	0.46	0.43	0.37	26.1	39.0	1.10
1	0.45	0.42	0.38	28.4	39.5	0.04
3	0.49	0.40	0.43	29.6	39.9	0.20
5	0.48	0.43	0.50	28.1	39.2	0.42
15	0.50	0.44	0.46	28.8	39.5	0.26
30	0.42	0.40	0.44	27.7	39.2	0.15

Table 5.3: Lorentzian Half-Width at Half-Maximum linewidth (HWHM), standard deviation of hyperfine fields σ and Fe^{3+} site populations f for the unmilled nanoferrite (0 h) and the milled Tet-NF composites (1, 3, 5, 15 and 30 h) in air and argon atmospheres. Tetrahedral (A), Octahedral (B) and superparamagnetic (Db) sites.

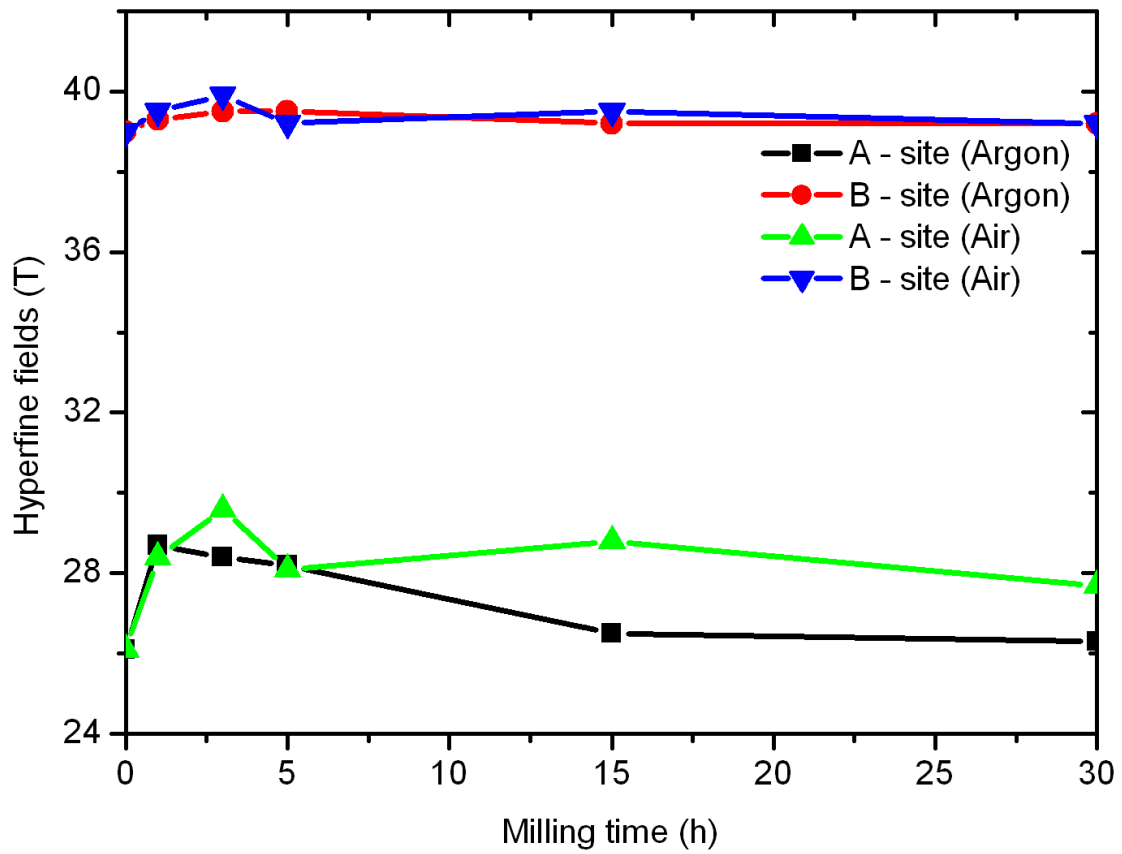| MT	HWHM	σ		f		
(h)	(mm/s)	(T)		(%)		
Argon	HWHM	σ_A	σ_B	f_A	f_B	f_{Dd}
	±0.04	±0.2	±0.6			
0	0.34	8.4	4.0	45.1	38.7	16.2
1	0.31	7.0	3.7	39.5	33.0	27.5
3	0.32	6.7	3.6	39.4	33.2	27.4
5	0.31	7.1	3.6	41.8	32.1	26.1
15	0.32	7.1	3.9	38.5	34.9	26.6
30	0.42	8.2	3.3	45.4	30.2	24.4
Air	HWHM	σ_A	σ_B	f_A	f_B	f_{Dd}
	±0.03	±0.1	±0.6			
0	0.34	8.4	4.0	45.1	38.7	16.2
1	0.32	7.1	3.7	42.3	31.9	25.8
3	0.34	7.0	3.3	44.3	28.5	27.2
5	0.32	6.4	3.7	35.2	36.0	28.8
15	0.31	6.6	3.5	41.2	29.8	29.0
30	0.34	6.5	3.6	34.8	32.9	32.3

Figure 5.5: Variation of hyperfine fields on the A and B sites for the unmilled nanoferrite (0 h) and the milled Tet-NF composites (1, 3, 5, 15 and 30 h) in air and argon atmospheres.

that the superparamagnetic phase increases more in the presence of oxygen than in an inert gas atmosphere.

5.2.3   Bioactivity of Tet-NF composites

The effectiveness of the Tet-NF composites against tetracycline in various bacteria cultures was investigated. Preliminary results show that the complexes are more effective than tetracycline [83]. The milling time is also found to be critical in the effectiveness of the Tet-NF composites in various bacteria cultures as illustrated in Figure 5.6. Details of the bacteria cultures used are not the subject of the current dissertation. However, we can clearly see that in many instances the region of the effectiveness (inhibition zone) of the Tet-NF is higher than for tetracycline on its own. Hence there is significant benefit in complexing tetracycline with nanoferrites.

5.3   Conclusions

We have successfully made Tet-NF composites by complexing $Mg_{0.5}Zn_{0.5}Fe_2O_4$ nano-ferrite made by glycol-thermal method with tetracycline-HCl via high energy ball milling. The starting materials were milled under air and argon atmospheres for 1, 3, 5, 15 and 30 h. The Tet-NF composites with cubic spinel structure formed after just 1 h of milling. We have observed an impurity peak around $2\theta = 58°$ for the 5 h air milled Tet-NF composite which is suspected to be due to oxidation of the drug. We have also obtained higher crystallite size after 30 h of milling in air atmosphere with no significant variation in the crystallite sizes of the argon milled Tet-NF composites. Mössbauer spectroscopy results show an increase in the doublet area in the first hour of milling in both air and argon atmospheres. We have obtained slightly larger isomer shifts on the tetrahedral (A) site than the octahedral (B) site for both milling atmospheres that is hardly affected by further milling. Hyperfine fields on the tetrahedral (A) sites were found to be more responsive to the milling time whilst the hyperfine fields on the octahedral (B) site seem to be least affected. Our results appear to show that tetracycline complexes more with ions on the tetrahedral (A) sites than on the octahedral (B) sites. Some preliminary results of Tet-NF bioactiv-
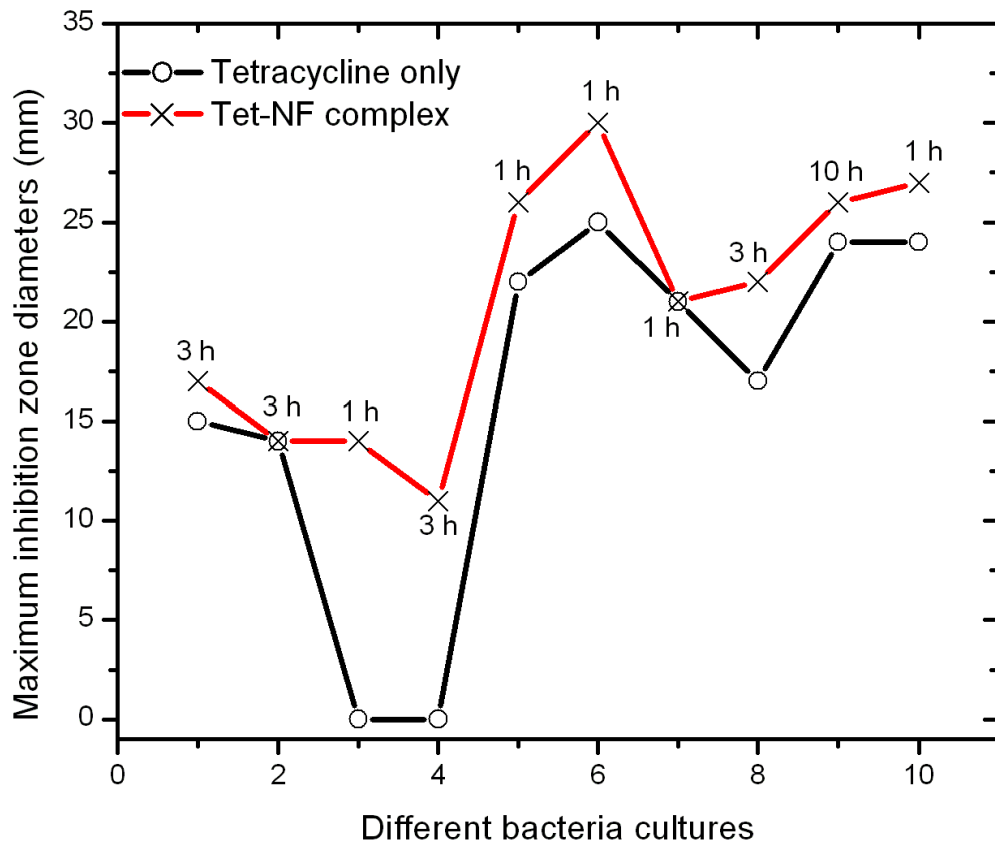
86

Figure 5.6: Preliminary results of the effectiveness of Tet-NF composites against tetracycline in various bacteria cultures.

ity have been presented which show potential applications of Tet-NF composites in combating bacteria.

Chapter 6

General conclusions

We have studied structural and magnetic properties of $Mg_{1-x}Zn_xFe_2O_4$ nanoferrites produced by the low temperature glycol-thermal technique. Structural properties were investigated by X-ray diffraction technique which gave information on crystallite sizes, lattice parameters and XRD density of the nanoferrites. In all compositions of the $Mg_{1-x}Zn_xFe_2O_4$ nanoferrites, single phase cubic spinel structure was obtained. Larger crystallite size of 22.24 nm $\pm$ 0.02 nm was obtained for $x = 0.6$ which is almost doubled for the low 10.60 nm $\pm$ 0.02 nm obtained for $x = 0.2$. Increasing the concentration of the Zn^{2+} ions resulted in an increase in the lattice parameters as expected because Zn^{2+} ions have a larger radii as compared to Mg^{2+} ions. A strong correlation was observed between XRD density (ρ_{XRD}) and x.

Room temperature Mössbauer spectra show ordered magnetic structures for $x \leq$ 0.7 and paramagnetic doublets for $x > 0.7$. Isomer shifts on A, B and doublet sites are consistent with Fe^{3+} ions. We have found that across the series the isomer shift values are less on A site than on B sites ($\delta_A < \delta_B$). The hyperfine fields based on the Lorentzian site analysis gradually decrease with increasing Zn content. Room temperature magnetization results show evidence of superparamagnetic behaviour of the nanoferrites. For $x = 0.8$, 0.9 and 1.0 reduced magnetizations are obtained which are consistent with the Mössbauer results. A peak in the room temperature saturation magnetization was also observed for $x = 0.5$ and the least magnetization is obtained for $x = 0.9$.

The sample at the composition $x = 0.5$ was complexed with tetracycline for

possible enhancement of the bioactivity of tetracycline against a range of bacteria. Hence we also investigated the structural and magnetic properties of tetracycline-nanoferrite (Tet-NF) composites made by high-energy ball milling. Complexing the planar structured tetracycline with the cubic spinel $Mg_{0.5}Zn_{0.5}Fe_2O_4$ nanoferrite resulted in essentially cubic spinel nanocomposites which suggest the incorporation of tetracycline into the spinel structure. The enhancement of average hyperfine fields are observed on both A and B sites. However, changes on A sites are more significant than on B sites. This suggest that tetracycline is affecting the A site more than the B site. Preliminary results also show significant enhancement of the bioactivity of the Tet-NF against a number of bacteria cultures. These results suggest further studies on the bioactivity of Tet-NF composites which are currently in progress.

Bibliography

[1] A. M. Gismelseed, K. A Mohammed, H. M. Widatallah, A. D. Al-Rawas, M. E. Elzain and A. A. Yousif, Journal of Physics: Conference Series **217** (2010) 012138.

[2] J. Z. Msomi and T. Moyo, Hyperfine Interactions **176** (2007) 93.

[3] S. Akhter, D. P. M. Saha, M. Mamun and A. Parveen, Materials Siences and Applications **2** (2011) 1675.

[4] A. B. Fuller, *Ferrites at Microwave Frequencies*, Peter Peregrinus Ltd, London (1987) 8–12.

[5] B. D. Cullity and C. D. Graham, *Introduction to Magnetic Materials*, John Wiley and Sons, New Jersey (2009) 178–180.

[6] J. Z. Msomi, *Synthesis, Structural and Magnetic Properties of Bulk and Nano-sized (Zn, Cd, Cu)$_{0.5}$Ni$_{0.5}$Fe$_2$O$_4$ and NiFe$_2$O$_4$ Ferrites*, University of KwaZulu-Natal (2007) PhD thesis.

[7] U. Müller, *Inorganic Structural Chemistry*, John Wiley and Sons, England (1993) 204–208.

[8] A.C.F.M. Costa, E. Tortella, M.R. Morelli and R.H.G.A. Kiminami, J. Magn. Magn. Mater. **256** (2003) 174.

[9] J. Z. Msomi and T. Moyo, Hyperfine Interactions **189** (2009) 151.

[10] D. Zhang, X. Zhang, X. Ni, J. Song and H. Zheng, Chem. Phys. Lett. **426** (2006) 120.

[11] L. Zhao, H. Zhang, Y. Xing, S. Song, S. Yu, W. Shi, X. Guo, J. Yang, Y. Lei and F. Cao, J. Sol. State Chem. **181** (2008) 245.

[12] J. Li, H. Yuan, G. Li, Y. Liu, and J. Leng, J. Magn. Magn Mater. **322** (2010) 3396.

[13] N. Amdouni, K. Zaghib, F. Gendron, A. Mauger, C.M. Julien, J. Magn. Magn Mater. **309** (2007) 100.

[14] I. Elahi, R. Zahira, K. Mehmood, A. Jamil, N. Amin, Afican Journal of Pure and Applied Chemistry **6** (2012) 1.

[15] E. E. Phillips, P. R. Byron, International Journal of Pharmaceutics **110** (1994) 9.

[16] www.irm.umn.edu

[17] J. M. D. Coey, *Magnetism and Magnetic Materials*, Cambridge university press, Cambridge (2010) 100–105, 195–219, 296–298, 330.

[18] D. Kim, D. E. Nikles and C. S. Brazel, Materials **3** (2010) 4051.

[19] T. Harasawa, R. suzuki, O. Shimizu, S. Olcer, and E. Eleftheriou, Transactions on Magnetics **46** (2010) 1894.

[20] M. D. Shultz, S. Calvin, P. P. Fatouros, S. A. Morrison and E. E. Carpenter, J. Magn. Magn Mater. **311** (2007) 464.

[21] E. Gopalan, I. Al-Omari, D. Kumar, Y Yoshida, P. Joy, M. Anantharaman, Applied Physics A Materials Science Processing **99** (2010) 497.

[22] J. Wang, C Zeng, Z. Peng and Q. Chen, Physica B: Condensed Matter **349** (2004) 124.

[23] G. Ott, J. Wrba and R. Lucke, J. Magn. Magn Mater. **254** (2003) 535.

[24] A. Daigle, J. Modest, A. L. Geiler, S. Gillette, Y. Chen, M. Geiler, B. Hu, S. Kim, K. Stopher, C. Vittoria and V G Harris, Nanotechnology **22** (2011) 305708.

[25] D. Bae, S. Kim, H. Lee and K. Han, Mater. Lett. **57** (2003) 1997.

[26] Q. Jiao, Y. Zhai, X. Bai, W. Zhang, J. Du and H. Zhai, Modern Physics Letters B **22** (2008) 1497.

[27] B. Viswanathan and V. R. K. Murthy, *Ferrite Materials: Science and Technology*, Narosa Publishing House (1990) 1–16.

[28] www.atsdr.cdc.gov

[29] www.epa.gov

[30] www.physics.sjsu.edu

[31] C. Kittel, *Introduction to Solid State Physics*, 7th edition, John Wiley and Sons (1996) 420–421, 424–425.

[32] N. W. Ashcroft and N. D. Mermin, *Solid State Physics*, Holt, Rinehart and Winston (1976) 650–652.

[33] J. Blakemore, *Solid State Physics*, W. B. Saunders Company (1970) 354–366, p. 50–53.

[34] www.cmp.liv.ac.uk

[35] P. Kopietz, L. Bartosch and F. Schütz, *Introduction to the Functional Renormalization Group*, Springer (2010) 30.

[36] www.doitpoms.ac.uk

[37] www.cnx.org

[38] www.springerimages.com

[39] H. M. I. Abdallah, *Synthesis, Magnetic and Electrical Characterizations of Nanoparticle Ferrites*, University of KwaZulu-Natal (2012) PhD thesis.

[40] C. M. Hurd, Contemporary Physics, **23** (1982) 469.

[41] A. P. Guimaraẽs, *Magnetism and Magnetic Resonance in Solids*, John Wiley and Sons (1998) 47–51.

[42] www.ebookbrowse.com

[43] T. Miyazaki and H. M. Jin, *The Physics of Ferromagnetism*, Springer-Verlag (2012) 287 – 314.

[44] www.energeticforum.com

[45] A. D Arelaro, E. Lima Jr, L. M. Rossi, P. K. Kiyohara and H. R. Rechenberg, J. Magn. Magn Mater. **320** (2008) 335.

[46] E. Manova, B. Kunev, D. Paneva, I. Mitov, L. Petrov, C. Estournès, C. D'Orléans, J. Rehspringer and M. Kurmoo, Chemical Materials **16** (2004) 5689.

[47] www.epswww.unm.edu

[48] Q. Song, *Size and Shape Controlled Synthesis and Superparamagnetic Properties of Spinel Ferrites Nanocrystals*, Georgia Institude of Technology (2005) PhD thesis.

[49] R. Wang, X. Lianga, Y. Penga, X. Fana and J. Lib, Journal of Ceramic Processing Research **10** (2009) 780.

[50] H. M. I. Abdallah, T. Moyo and J. Z. Msomi, Journal of Physics: Conference Series **217** (2010) 012141.

[51] H. M. I. Abdallah, T. Moyo and J. Z. Msomi, Journal of Superconductivity and Novel Magnetism **24** (2011) 669.

[52] W. B. Dlamini, ^{57}Fe *Mössbauer of* $^{57}Mn^*$ *implanted III-V semiconductor InP and InAs*, School of Chemistry and Physics, University of KwaZulu-Natal (2011) MSc dissertation.

[53] N. N. Greenwood and T. C. Gibb, *Mössbauer Spectroscopy*, Chapman and Hall, London, UK (1971) 16–65.

[54] G. K. Wertheim, *Mössbauer Effect: Principles and Applications*, Academic Press Inc., New York, London (1964) 3–82.

[55] www.chemwiki.ucdavis.edu

[56] www.rsc.org

[57] www.phys.ksu.edu

[58] www.serc.carleton.edu

[59] G. N. Belozerski, *Mössbauer Studies of Surface Layers*, Elsevier Science Publishers B.V, Amsterdam, London, New York, Tokyo (1993) 5–29.

[60] www.nanomagnetics.org

[61] A. Niazi, P. Poddar and A. K. Rastogi, Current Science **79** (2000) 99.

[62] www.lakeshore.com

[63] B. K. Nath, P. K. Chakrabarti, S. Das, U. Kumar, P. K. Mukhopadhyay and D. Das, Journal of Surface Science and Technology **21** (2005) 169 .

[64] R. Dunlap, A. Alghamdi, J. OŠBrien and S. Penney, Journal of Alloys and Compounds **365** (2004) 84.

[65] A. Y Lipare, P. N. Vasambekar and A. S. Vaingankar, Bulletin of Material Science **26** (2003) 493.

[66] S. Sharma and N. D. Sharma, Indian Journal of Pure and Applied Physics **44** (2006) 220.

[67] B. P. Ladgaonkar, P. N. Vasambekar and A. S. Vain-gankar, Turkish Journal of Physics **25** (2001) 129.

[68] D. Ravinder and P. Vijaya Bhasker Reddy, J. Magn. Magn Mater. **263** (2003) 127.

[69] S. S. Bellad, S. C. Watawe and B. K. Chougule, J. Magn. Magn. Mater. **195** (1999) 57.

[70] N. Rezlescu, L. Sachelarie, L. Rezlescu, P. D. Popa, Crystal Research and Technology **36** (2001) 157.

[71] K. Roumaih, R. Manapov, E. Sadykov and A. Pyataev, J. Magn. Magn Mater. **288** (2005) 267.

[72] B. Parvatheeswara Rao, P. S. V. Subba Rao, G. V. S. Murthy and K. H. Rao, J. Magn. Mater. **268** (2003) 315.

[73] T. Moyo, J. Msomi and K. Bharuth-Ram, Hyperfine Interactions **136** (2001) 579.

[74] M. Sertkol, Y. Köseoğlu, A. Baykal, H. Kavas and A. C. Basaran, J. Magn. Magn Mater. **311** (2009) 157.

[75] M. Ahmed, J. Magn. Magn Mater. **311** (2010) 763.

[76] N. E. Fenineche, R. Hamzaoui and O. El Kedim, Materials Letters **57** (2003) 4165.

[77] www.wikepedia.org

[78] www.chcwm.com

[79] D. S. Mathew and R. S. Juang, Chemical Engineering Journal **129** (2007) 51.

[80] Y. Ichiyanagi, M. Kubota, S. Moritake, Y. Kanazawa, T. Yamada and T. Uehashi, J. Magn. Magn Mater. **310** (2007) 2378.

[81] M. L. Branham, T. Moyo, H. M. I. Adballah and P. Masina, European Journal of Pharmaceutics and Biopharmaceutics, DOI: 10.1016/j.ejpb.2012.09.017.

[82] D. Fang, C.G. Lee, and B. H. Koo, Metals and Materials International **13** PART 2 (2007) 165-170.

[83] M. L. Branham, P. Masina, C. Mocktar, T. Govender and T. Moyo, Poster presentation, School of Pharmarcy and Pharmacology, University of KwaZulu-Natal (2012).